Geodetic SAR Tomography

Zhu, Xiao Xiang; Montazeri, Sina; Gisinger, Christoph; Hanssen, Ramon F.; Bamler, Richard

DOI
10.1109/TGRS.2015.2448686

Publication date
2016

Document Version
Final published version

Published in
IEEE Transactions on Geoscience and Remote Sensing

Geodetic SAR Tomography

Xiao Xiang Zhu, *Senior Member, IEEE*, Sina Montazeri, Christoph Gisinger, Ramon F. Hanssen, *Senior Member, IEEE*, and Richard Bamler, *Fellow, IEEE*

***Abstract*—In this paper, we propose a framework referred to as "geodetic synthetic aperture radar (SAR) tomography" that fuses the SAR imaging geodesy and tomographic SAR inversion (TomoSAR) approaches to obtain *absolute* 3-D positions of a large amount of natural scatterers. The methodology is applied on four very high resolution TerraSAR-X spotlight image stacks acquired over the city of Berlin. Since all the TomoSAR estimates are relative to the same reference point object whose absolute 3-D positions are retrieved by means of stereo SAR, the point clouds reconstructed using data acquired from different viewing angles can be geodetically fused. To assess the accuracy of the position estimates, the resulting absolute shadow-free 3-D TomoSAR point clouds are compared with a digital surface model obtained by airborne LiDAR. It is demonstrated that an *absolute positioning* accuracy of around 20 cm and a meter-order *relative positioning* accuracy can be achieved by the proposed framework using TerraSAR-X data.**

***Index Terms*—Absolute positioning, geodetic SAR tomography, geodetical fusion, SAR geodesy, SAR tomography, stereo SAR, synthetic aperture radar (SAR), TerraSAR-X.**

I. Introduction

SPACEBORNE tomographic synthetic aperture radar (SAR) inversion (TomoSAR) [1]–[9] uses stacks of SAR images acquired at slightly different positions over a certain time period in a repeat–pass manner, like all other advanced InSAR techniques, such as persistent scatterer interferometry (PSI) [10]–[14], small baseline subset (SBAS) [15]–[17], SqueeSAR [18]–[20], and CEASAR [21]. They all aim at retrieving the 3-D position and the parameters of the undergoing motion of point, surface, and/or volumetric scatterers. Among them, TomoSAR is the only technique that can reconstruct nontrivial reflectivity profiles along the third native coordinate of SAR—elevation s—for each azimuth–range $(x - r)$ pixel. In particular, using stacked very high resolution (VHR) SAR images delivered by modern spaceborne SAR sensors, TomoSAR allows us to retrieve not only the most detailed 3-D geometrical shape but also the undergoing temporal motion of individual buildings and urban infrastructures in the centimeter or even millimeter scale [4], [5], [22], [23]. The resulting 4-D point clouds have a point (scatterer) density that is comparable to LiDAR. Experiments using TerraSAR-X high-resolution spotlight data stacks show that a scatterer density on the order of one million points per square kilometers can be achieved by TomoSAR [24]. However, similar to conventional InSAR and PSI, the elevation and deformation rates are estimated with respect to a previously chosen reference point that makes them *relative 3-D* estimates [25]–[27].

Another attractive feature of modern SAR sensors, in particular of TerraSAR-X and TanDEM-X, is the precise orbit determination and high geometrical localization accuracy. After compensating for the most prominent geodynamic and atmospheric error sources, the *absolute* 2-D (range and azimuth) positions of targets such as corner reflectors and persistent scatterers can be estimated to centimeter-level accuracy—a method called "SAR imaging geodesy" [28], [29]. Moreover, using two or more SAR observations acquired from different satellite orbits, their *absolute* 3-D positions can be retrieved by means of stereo SAR [30]. However, common scatterers that appear in SAR images acquired from different geometries, in particular from cross heading orbits, are very rare. This limits the application in 3-D absolute scattering positioning.

In this paper, we propose a framework referred to as "geodetic TomoSAR" that fuses the SAR image geodesy and TomoSAR approaches to obtain *absolute 3-D positions* of a large amount of natural scatterers. We work on four stacks of TerraSAR-X high-resolution spotlight images over the city of Berlin, among them two are acquired from ascending orbits and two from descending ones. First, tens of opportunistic (or natural) point scatterers that appear in all image stacks are manually identified. Their *absolute* 2-D SAR range and azimuth positions are calculated using imaging geodesy by compensating all the error sources, and their absolute 3-D positions are then calculated using stereo SAR. the most precisely localized point target is then chosen as reference point for the follow-on TomoSAR processing. Since the TomoSAR estimates are relative to the identical reference point whose absolute 3-D positions are known, the resulting point clouds are geodetically fused. Finally, to assess the position estimates, the resulting absolute 3-D TomoSAR point clouds are compared with a

Manuscript received May 14, 2015; revised June 3, 2015; accepted June 12, 2015. This work was supported in part by the Helmholtz Association under the framework of the Young Investigators Group "SiPEO" (VH-NG-1018). This work is also part of the project "6.08 4-D City" funded by the IGSSE of Technische Universität München and the German Aerospace Center (DLR, Förderkennzeichen 50EE1417). This project was also supported by the Gauss Centre for Supercomputing e.V. which provided computing time on the GCS Supercomputer SuperMUC at the Leibniz Supercomputing Centre (LRZ). The LiDAR data used in this work were provided by "Land Berlin" and "Business Location Service", supported by "Europäischer Fonds für Regionale Entwicklung" (EFRE).

X. X. Zhu is with the Remote Sensing Technology Institute, German Aerospace Center, 82234 Wessling, Germany, and also with the Signal Processing for Earth Observation (SiPEO), Technische Universität München, 80333 Munich, Germany (e-mail: xiao.zhu@dlr.de).

S. Montazeri is with the Remote Sensing Technology Institute, German Aerospace Center, 82234 Wessling, Germany.

C. Gisinger is with the Institute for Astronomical and Physical Geodesy, Technische Universität München, 80290 Munich, Germany.

R. F. Hanssen is with the Department of Geoscience and Remote Sensing, Delft University of Technology, 2628 CN Delft, The Netherlands.

R. Bamler is with the Remote Sensing Technology Institute, German Aerospace Center, D-82234 Wessling, Germany, and also with the Institute for Remote Sensing Technology, Technische Universität München, 80333 Munich, Germany.

Color versions of one or more of the figures in this paper are available online at http://ieeexplore.ieee.org.

Digital Object Identifier 10.1109/TGRS.2015.2448686

digital surface model (DSM) obtained by airborne LiDAR. Experimental results demonstrate that the absolute positioning accuracy using TerraSAR-X is around 20 cm. The elevation estimation accuracy of TomoSAR depends on the number of the used images, SNR, baseline distribution, orbit height, and wavelength. In our experiments using TerraSAR-X, it is around 1 m [31].

II. Stereo SAR

A. SAR Imaging Geodesy for Absolute Ranging

The general imaging principle of SAR is based on the transmission of pulses and the reception of their echoes reflected back from the surface. Therefore, the location of a pixel in a radar image corresponds to the two-way round-trip time t_R (= range) as well as the mean time of transmission and reception t_A (= azimuth). Since the position of the satellite with respect to time is known from precise orbit determination, the azimuth is referred to an absolute location in 3-D space. The geometric distance R from this satellite position to the surface is obtained by scaling the two-way round-trip time with the velocity of light c.

In the case of a point scatterer, the two radar observations, i.e., the azimuth time and the geometric range, can be extracted from the focused SAR image through point target analysis (PTA), which yields the center coordinates of the scatterer's signature at subpixel level. If the errors present in this type of observations (atmospheric signal delays including ionospheric and tropospheric delays, geodynamic displacements such as solid Earth tides, continental drift, atmosphere pressure loading, ocean tidal loading, pole tides, ocean pole tides, and atmosphere tidal loading) are corrected by external models and the remaining unknown effects, e.g., time delays induced by cables and electronics, are calibrated for, the outcome are absolute 2-D radar observations.

For TerraSAR-X and TanDEM-X, this whole process has been mastered down to the 1–2 cm level [32]. It involves an accurate SAR processor to generate the focused SAR images, the PTA to extract the radar coordinates, the computation of the external corrections, and the geometrical calibration [32]. Since the process combines correction principles used in geodesy with SAR, we refer to it as SAR imaging geodesy [28]. The following provides a short summary on important elements of the process, and the reader interested in the details can find them in [28], [32].

In order to generate SAR images that are accurately focused in zero-Doppler geometry, the TerraSAR-X multimode SAR processor (TMSP) [33] avoids approximations often used to reduce the computational effort, e.g., the stop–go approximation, which assumes a static satellite during the transmission and reception of one pulse. Furthermore, effects such as the nonzero duration of the pulses are taken into account. For the external corrections, we distinguish between the signal propagation delays due to the atmosphere and the geodynamical effects (solid Earth tides, plate tectonics, ocean loading, atmospheric loading, etc.), causing a displacement of a target on ground. The geodynamic effects are considered by models following the conventions issued by the International Earth Rotation and Reference Systems Service (IERS) [34], whereas the atmosphere is corrected through path delays derived from complementary Global Navigation Satellite System (GNSS) observations. Thus, the concept of separating the atmospheric delay into a nondispersive part (usually called tropospheric delay—even if it involves also contributions from other atmosphere layers) and a dispersive part (ionospheric delay) which is well established in the field of GNSS [35] can be adapted to SAR.

It is worth to mention for medium-resolution sensors, such as Sentinel-1, the positioning capability is less precise than for high-resolution sensors. In fact, a Sentinel-1 artificial corner reflector needs to be 4.5 m large, which is unrealistic, in order to achieve 1-cm range accuracy. Shoebox-sized compact active transponders would be a convenient and highly demanded alternative [36].

Based on these thoroughly corrected 2-D observations, our stereo SAR approach allows the straightforward retrieval of absolute 3-D coordinates by combining sets of range and azimuth observations of a target in a joint parameter estimation.

B. Stereo SAR for Absolute 3-D Positioning of Corner Reflectors or Persistent Scatterers

The details as well as the validation of the stereo SAR method outlined in this section are given in [37]. Its analysis was carried out for TerraSAR-X and TanDEM-X data of our corner reflectors located at the geodetic observatories Wettzell (Germany) and Metsähovi (Finland). The reference coordinates of both reflectors are known from onsite geodetic surveying with accuracy better than 5 mm, and the comparison with the solution computed by stereo SAR showed differences at the 2–3-cm level [37].

The geometry of a SAR observation of a single point target at zero-Doppler location is given by the well-known range-Doppler equation system [38], i.e.,

$$|\mathbf{X}_S - \mathbf{X}_T| - R = 0 \tag{1}$$

$$\frac{\dot{\mathbf{X}}_S(\mathbf{X}_T - \mathbf{X}_S)}{|\dot{\mathbf{X}}_S||\mathbf{X}_T - \mathbf{X}_S|} = 0 \tag{2}$$

where $\mathbf{X}_s$ and $\dot{\mathbf{X}}_s$ are the position and velocity vectors of the sensor with respect to the azimuth time t_A, $\mathbf{X}_T$ denotes the unknown position vector of the target, and R is the observed range derived from the two-way round-trip time after compensation of all system and atmospheric delays. If the relationship between the sensor trajectory during an acquisition (position and velocity) and the azimuth time is expressed by an analytical model, e.g., polynomials, and introduced into the range-Doppler equations, the unknown target position $\mathbf{X}_T$ can be resolved in absolute 3-D by combining at least two acquisitions. In terms of geometry, this corresponds to the intersection of two or more circles that are perpendicularly oriented with respect to the sensor trajectories since the target is considered to be at zero-Doppler location (see Fig. 1).

The mathematical problem becomes overdetermined for two or more radar acquisitions because every acquisition i provides two equations (1) and (2) that relate the observations $t_{A,i}$ and $t_{R,i}$ with the three target coordinates $\mathbf{X}_T = [x\ y\ z]$. However, an optimal solution to this problem can be found by applying general least squares parameter estimation [37]. This allows a straightforward computation of absolute 3-D coordinates in the

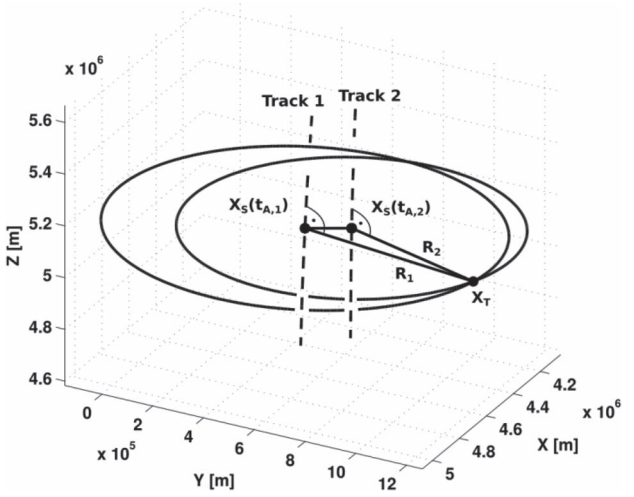

Fig. 1. Graphical representation of a stereo SAR acquisition for a target at zero-Doppler location. Note that due to the availability of repeat–pass data stacks, we use multiple images from the same geometry in stereo SAR configuration for a more accurate and robust absolute 3-D location estimation.

global reference frame of the satellite orbit, and all observations taken from orbit tracks with visibility on the target can be combined into a single estimate. In addition to the actual coordinate solution, the parameter estimation provides the corresponding standard deviations that allow the quality analysis of the solution. The standard deviations are influenced by the noise of the observations, the intersection geometry given by the separation of the orbit tracks (= stereo baseline), and the total amount of acquisition used to compute the solution.

In order to apply the stereo SAR method with TerraSAR-X in practice, the following steps have to be performed.

1) Focusing of the TerraSAR-X image by the TMSP. The step is fulfilled by ordering the TerraSAR-X L1B data, which provides not only the accurately focused single-look slant range complex (SLC) images but also extensive metainformation [39]. This metainformation includes the trajectory of the SAR antenna phase center in the International Terrestrial Reference Frame (ITRF) 2008, which is described by discrete position and velocity vectors (10-s sampling interval). Polynomials are used to interpolate the trajectory from the state vectors of the science orbit.
2) Locating the maxima of the point scatterer responses visible in the images taken from different orbit tracks by using PTA. The PTA algorithm must avoid aliasing and employ best practice interpolation.
3) Computation of the external radar corrections introduced in Section II-A according to the time and the observation geometry of every acquisition.
4) Stereo SAR processing using the range and azimuth observations of Step 2 corrected by the results of Step 3, as well as the polynomial trajectory models obtained in Step 1.

Note that Steps 3 and 4 have to be performed in iteration: An initial 3-D position is computed without correcting the observation data. This solution is introduced into the correction computation, which yields a first set of corrections. After repeating this process one to two times, both the corrections and the position solution become stable, and the final result is achieved.

III. TomoSAR

TomoSAR, including SAR tomography and differential SAR tomography, uses stacks of SAR images taken from slightly different positions over a long period in a repeat–pass manner and uses the stacks to reconstruct the 3-D positions of coherent objects and their undergoing motion by means of spectral estimation. According to the scattering mechanism, the coherent targets, i.e., the signal, to be resolved can be categorized as discrete scatterers and volumetric scatterers. The reflectivity along elevation of discrete scatterers can be characterized by several δ-functions, i.e., the signal can be described by a deterministic model with a few parameters. Volumetric scatterers have a continuous backscatter profile associated with completely random scattering phases, i.e., the signal can only be described by stochastic models. Our target application is urban infrastructure monitoring, i.e., the resolution of discrete scatterers with motion. For tomographic SAR reconstruction of distributed scatterers, the readers are recommended to consult [40], [41].

Among various TomoSAR system models, differential SAR tomography was originally proposed in [2] for estimating linear motion of multiple scatterers inside a pixel. Motion, however, is often nonlinear (periodic, accelerating, stepwise, etc.). Therefore, conventional differential SAR tomography has been extended to estimate multicomponent nonlinear motion in [5] by means of the generalized "time warp" method. It rewrites the D-TomoSAR system model to an $M+1$-dimensional standard spectral estimation problem, where M indicates the user-defined motion model order and hence enables the motion estimation for all possible complex motion models. In this section, this generalized model will be briefly described.

The focused complex-valued measurement g_n at an azimuth–range pixel for the nth acquisition at time t_n $(n = 1, \ldots, N)$ is [3]

$$g_n = \int_{\Delta s} \gamma(s) \exp\left(-j2\pi\left(\xi_n s + 2d(s,t_n)/\lambda\right)\right) ds \qquad (3)$$

where $\gamma(s)$ represents the reflectivity function along elevation s with an extent of Δs, and $\xi_n = -2b_n/(\lambda r)$ is the spatial (elevation) frequency proportional to the respective aperture position (baseline) b_n, with λ being the wavelength and r being the range. $d(s,t_n)$ is the line-of-sight (LOS) motion as a function of elevation and time. The motion relative to the master acquisition may be modeled using a linear combination of M base functions $\tau_m(t_n)$ [5], i.e.,

$$d(s,t_n) = \sum_{m=1}^{M} p_m(s)\tau_m(t_n) \qquad (4)$$

where $p_m(s)$ is the corresponding motion coefficient to be estimated. Later, we will show that $\tau_m(t_n)$ can be interpreted as a warped time variable if we choose the units of the coefficients

appropriately. The choice of the base functions depends on the underlying physical motion processes, e.g., linear, seasonal, step function, temperature history, or even measured GPS deformation series of ground control points.

Let us define the mth temporal frequency component at t_n as $\eta_{m,n} = 2\tau_m(t_n)/\lambda$. Then, (3) can be rewritten as an $M+1$-dimensional Fourier transform of $\gamma(s)\delta(p_1 - p_1(s), \ldots, p_M - p_M(s))$, which is a delta line in the $M+1$ elevation-motion parameter space, i.e., [5]

$$g_n = \int_{\Delta p_M} \cdots \int_{\Delta p_1} \int_{\Delta s} \gamma(s)\delta\left(p_1 - p_1(s), \ldots, p_M - p_M(s)\right) \cdot \exp\left(-j2\pi(\xi_n s + \eta_{1,n}p_1 + \cdots + \eta_{M,n}p_M)\right) \times ds dp_1, \ldots, dp_M,\ n = 1, \ldots, N. \quad (5)$$

After discretizing (5) along s and motion parameter space, in the presence of noise $\boldsymbol{\varepsilon}$, the discrete-TomoSAR system model can be written as

$$\mathbf{g} = \mathbf{R}\boldsymbol{\gamma} + \boldsymbol{\varepsilon} \quad (6)$$

where $\mathbf{g}$ is the measurement vector with N elements, $\boldsymbol{\gamma}$ is the reflectivity function along elevati on uniformly sampled along elevation s_l $(l = 1, \ldots, L)$ and motion parameter space p_{m,l_m} $(l_m = 1, \ldots, L_m)$. $\mathbf{R}$ is an irregularly sampled M-dimensional discrete Fourier transform mapping matrix sampled at ξ_n and $\eta_{m,n}$. In practice, $\mathbf{R}$ and $\boldsymbol{\gamma}$ are reshaped to 2-D matrices, with a dimension of $N \times (L \times L_1 \times \cdots L_M)$. This renders tomographic SAR inversion a higher dimensional spectral estimation problem that can be again solved by the well-established spectral estimation methods. For more details, the readers are recommended to consult [5].

In our test sites, the following two component motion base functions, i.e., $\mathrm{M} = 2$, are assumed.

- *Linear motion*: $\eta_{1,n} = 2t_n/\lambda$, and the coefficient $p_1(s)$ stands for the LOS velocity (v) as a function of s.
- *Seasonal motion*: $\eta_{2,n} = 2\tau_2(t_n)/\lambda$ where $\tau_2(t_n) = \sin(2\pi(t_n - t_0))$ can be interpreted as a warped time variable modeling the seasonal movement evolving over time, and $p_2(s)$ stands for the amplitude (a) of the periodic motion; t_0 is the initial phase offset.

IV. Geodetic SAR Tomography

Here, we will introduce the proposed framework *geodetic SAR tomography*, which consists of four main steps, namely, identification of reference point candidates, absolute positioning of reference point candidates, TomoSAR processing, and fusion of geodetic point clouds. To make the procedure more accessible for the readers, we explain the framework together with practical examples.

A. Data Sets

In this paper, the investigated test site includes the central area of the city of Berlin, Germany. The available data set consists of four stacks of TerraSAR-X VHR spotlight images acquired with a range bandwidth of 300 MHz. The images have an azimuth resolution of 1.1 m and a slant-range resolution of 0.6 m covering an area of 10 km × 5 km. Two stacks are acquired from descending orbits with images recorded at 05:20 Coordinated Universal Time (UTC), and two stacks are acquired from ascending tracks with images recorded at 16:50 UTC. Fig. 2 shows the mean scene coverage of individual stacks overlaid on the optical image of Berlin. Furthermore, the details about the system parameters and properties of each stack are summarized in Table I.

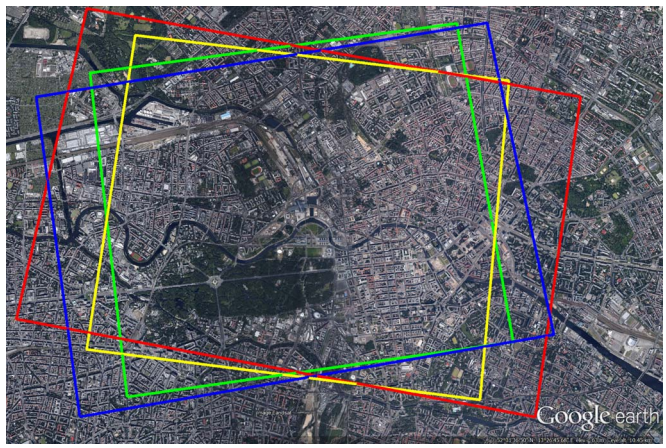

Fig. 2. Optical image of the city of Berlin (Google Earth). Rectangles mark the coverage of the four TerraSAR-X data stacks.

TABLE I
Acquisition Parameters of Each Stack Including the Average Incidence Angle, the Flying Direction or Azimuth, the Track Type and the Number of Available Images

Beam	Incidence angle	Heading angle	Track type	Nr. of Images
57	41.9°	350.3°	Ascending	102
85	51.1°	352°	Ascending	111
42	36.1°	190.6°	Descending	109
99	54.7°	187.2°	Descending	138

Since Berlin is regularly monitored by TerraSAR-X, a large number of images are available for each stack ranging from 102 to 138 with a time span of approximately five years from February 2008 to March 2013 with the acquisition repeat cycle of 11 days. The four stacks consist of noncoregistered complex images.

In addition to the TerraSAR-X data sets, a point cloud of the test area obtained from aerial laser scanning is available (provided by "Land Berlin" and "Business Location Service," supported by "Europäischer Fonds für Regionale Entwicklung"). This data set is used to construct a DSM, which serves as a reference for the localization accuracy analysis of the TomoSAR point clouds. The LiDAR point cloud corresponding to the Reichstagsgebäude, Berlin, Germany, is visualized in Fig. 3.

B. Absolute Positioning of the Reference Point

As a characteristic of all interferometric SAR techniques, the height and deformation updates are estimated relative to a reference point. Although special care is taken to choose the reference point in an area close to the reference digital elevation model (DEM) and most plausibly not affected by

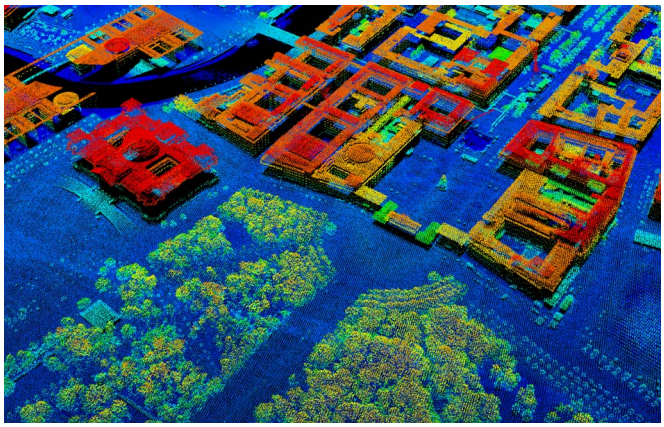

Fig. 3. LiDAR point cloud of a small area in Berlin in UTM coordinate system based on WGS 84 data. High absolute localization accuracy, on the order of 10 cm, makes the point cloud an excellent source to serve as a reliable reference surface model.

deformation, this however cannot be fully guaranteed and leads to complication in interpretation of the final results. Moreover, the exact 3-D position of the reference point is not known. Therefore, it is more likely that the final geocoded results will show offsets or even small scaling effect with respect to their true positions. The latter can also be problematic when it is desired to fuse the results obtained from different (same-heading or cross-heading) tracks in order to produce shadow-free point clouds. In this case, a lack of knowledge about the exact height of the reference point leads to inconsistencies between the point clouds [42]–[44].

In the following, the approach to select and absolutely localize natural point scatterers in SAR images is reported. The exact 3-D positions of the points are achieved with the stereo SAR method explained in Section II. Finally, the point with the highest quality is used as the reference point in the TomoSAR processing of all the four stacks which is extensively treated in Section IV-C.

1) Identification of Reference Point Candidates: The point targets, on which the 3-D stereo SAR reconstruction is performed, should have certain characteristics to be considered suitable reference point candidates. The criteria are the following.

- The target should be located in an isolated area.
- The target should be a single scatterer of high SNR, which is visible through the entire stack of SAR images.
- The target should be visible, at least, in two stacks of images acquired from different geometries.

The first condition should be satisfied in order to minimize the impact of interference caused by neighboring targets' responses on the reference candidate point. This is met by visual inspection of the mean amplitude image of each stack and the corresponding optical image of the scene to identify isolated targets.

The second condition ensures that the later tomographic reconstruction reaches in a higher 3-D localization as these points will also be served as reference points while forming differential observations. This is dealt with by calculation of the normalized amplitude dispersion index [10].

The third condition is vital from the radargrammetric point of view. Although, in optical imagery, selection of identical targets is commonly carried out with well-established algorithms such as scale-invariant feature transform (SIFT) [45] and Kanade–Lucas–Tomasi feature tracker [46], in SAR images, this cannot be done due to the existence of speckle [47]. For this reason and also considering the low number of candidates, in this paper, identical targets were selected manually by visual investigation of mean amplitude images of different stacks.

2) Absolute Positioning of the Reference Point: The outcome of the aforementioned procedure is eight point scatterers chosen from the central area of the city of Berlin (see Figs. 4 and 5). All of the scatterers are assumed the base of lamp posts located in the area, which typically have cylinder shapes that can reflect back radar signals from all illumination angles as shown in the right plot of Fig. 4. The scatterers are from three different types categorized based on the combination of geometry used for 3-D positioning, namely, ascending–ascending (AA), descending–descending (DD), and ascending–descending (AD). Fig. 6 shows the two different stereo orbit configurations that are used for point scatterers in Berlin. For each target, the time coordinates are retrieved by PTA from a number of SAR images in the stack. These time measurements are first corrected and then used in the zero-Doppler equations, outlined in Section II, to retrieve the 3-D coordinates. Table II gives an overview of data-take configurations, the time period within which the time coordinates were measured and the number of images used in PTA.

Among the candidates reported in Table II and visualized in Figs. 4 and 5, the one with the highest quality, i.e., the lowest 3-D standard deviation is selected as the reference point for TomoSAR processing of all the SAR image stacks. The stability of the results depends on the geometry of the observations, the number of observations, and the SNR of the targets. The geometrical configuration is the most important factor as for AD geometry the intersection occurs at almost 90° angle providing a well-conditioned system of equations. This effect can be clearly seen in Fig. 6(b), whereas a large baseline between the ascending and the descending acquisitions is achievable. On the other hand, AA or DD configurations [see Fig. 6(a)] result in a more ill-posed system due to a rather small baseline. In order to support the aforementioned discussion, the coordinate standard deviations of the scatterers are plotted in Fig. 7 (left subfigure). The horizontal axis consists of the names of the scatterers with subscripts denoting the geometry used for the 3-D positioning. The vertical axis describes the standard deviation values ranging from 1 to 9 cm, which are at least one order of magnitude better than the relative estimates achieved by repeat–pass InSAR. In addition, the graph demonstrates that the standard deviation values are lower in the x-direction. Moreover, as it was expected, the results from P_{AD1} and P_{AD2}, which are calculated from the cross-heading orbits, are more precise than the other points. It is worth mentioning that restricting the quality control of estimates solely based on the standard deviations may not be a reliable criterion. This is mainly due to the presence of covariance between the coordinate stochastics. Therefore, it is meaningful to analyze the error ellipsoid that is obtained

Fig. 4. (Left) Selected reference point candidates visualized as red dots in the optical image of Berlin (Google Earth). All of the candidates are assumed base of lamp posts. (Right) Photograph of one of such lamp posts in Berlin.

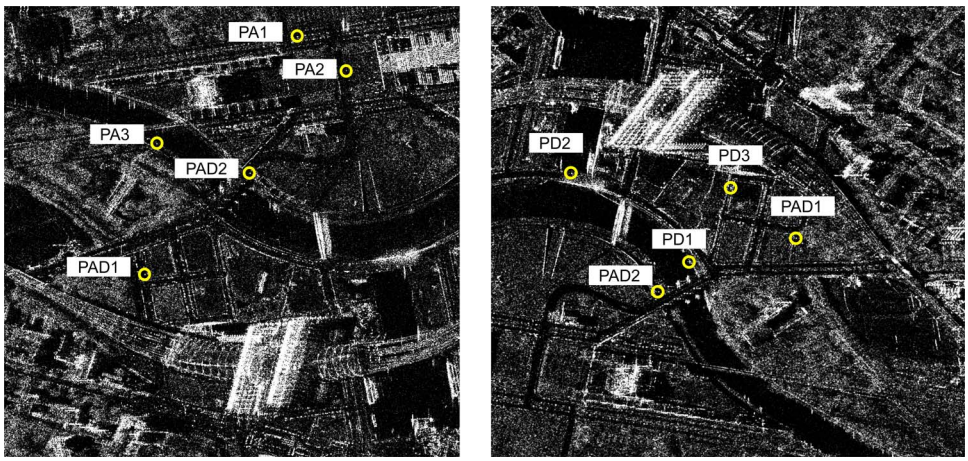

Fig. 5. Selected reference point candidates distinguished with yellow circles in the SAR images taken from the ascending and descending geometries with an incidence angle between 36° and 55°, as detailed in Table I.

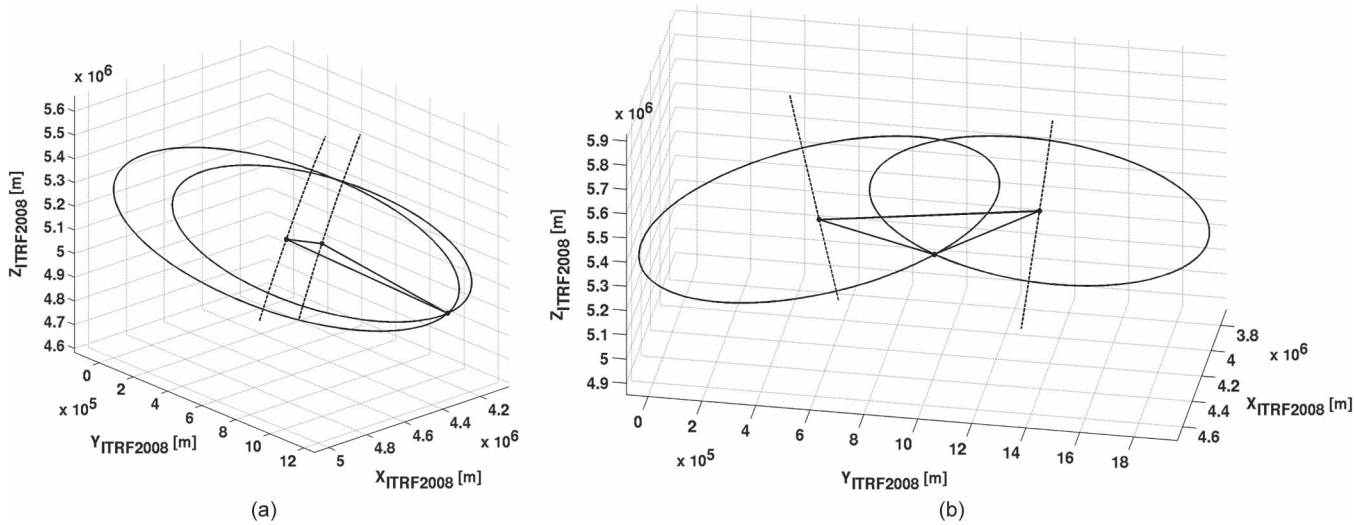

Fig. 6. Different orbit stereo configurations taken into account for 3-D scatterer reconstruction in Berlin. (a) Same heading orbits. (b) Cross-heading orbits.

by transformation of the posterior variance–covariance matrix of the estimates to the uncorrelated diagonal matrix of the eigenvalues based on eigenvector decomposition. In this case, the diagonal elements of the decomposed matrix represent the stochastics in the inherent SAR coordinate system. The mentioned approach was carried out on the variance–covariance

TABLE II
DATA TAKE CONFIGURATION FOR THE SELECTED NATURAL POINT SCATTERERS

Scatterer	Geometry	Period	Nr. of Data-takes	Beams
P_{AD1}	AD	2008-2011	33	42,57
P_{AD2}	AD	2008-2011	30	42,57
P_{A1}	AA	2008-2011	22	57,85
P_{A2}	AA	2010-2012	9	57,85
P_{A3}	AA	2010-2012	6	57,85
P_{D1}	DD	2010-2011	11	42,99
P_{D2}	DD	2010-2011	8	42,99
P_{D3}	DD	2010-2011	11	42,99

matrix of each point, and the result is plotted in Fig. 7 (right subfigure) where σ_r, σ_a, and σ_s denote the ellipsoid axes that orient themselves with respect to the range, the azimuth, and the elevation of the SAR geometry, respectively. It is observed that, for the scatterers, which are localized from the same-heading geometries, the range component is minimal followed by azimuth, whereas the highest uncertainties are allocated to elevation components varying from 4 to 14 cm. However, it is seen that due to the almost optimum geometry configuration of cross-heading tracks, the elevation components of P_{AD1} and P_{AD2} have the smallest value better than 2 cm.

Based on the given discussion, the matter of configuration leads to discarding the point targets identified from the same-heading tracks narrowing the selection between P_{AD1} and P_{AD2}. Among them, P_{AD1} was selected as the reference point since it has slightly better precision, and it was also visible in all the four stacks. Fig. 8 shows the selected target in the mean amplitude images of one ascending and one descending TerraSAR-X spotlight image. The target is a lamp pole in a pedestrian area near the Berlin central station. Its absolute positions in the ITRF 2008 are as follows:

$$[X\ \ YZ] = [3783630.014 \pm 0.010\ \mathrm{m}\ 899035.0040 \pm 0.010\ \mathrm{m}\ 5038487.589 \pm 0.011\ \mathrm{m}].$$

It has to be emphasized that the listed 1-cm level uncertainties refer to the variance–covariance information provided by the position computation with stereo SAR. Thus, these values are a measure for the consistency of the stereo-based scatterer retrieval. It must be considered however that the satellite illuminates different sides of the lamp post from ascending and descending orbits. Regarding the absolute accuracy of the reference point, we expect a bias on the order of 20 cm, which depends on the diameter of the lamp post. We will analyze this possible bias in Section IV-D.

C. Tomographic Processing

After choosing the aforementioned absolutely geo-positioned scatterer as the reference point, the InSAR stacking and TomoSAR processing were done by the PSI-GENESIS [11] and Tomo-GENESIS system [48], [49] of the Remote Sensing Technology Institute of DLR, respectively.

The Tomo-GENESIS processing chain consists of three main steps, namely, preprocessing, tomographic processing, and fusion of point clouds. In this paper, mainly the first two steps are concerned, which are briefly outlined as follows. Furthermore, instead of geometrical fusion of point clouds as previously used in Tomo-GENESIS, a geodetical fusion method will be introduced.

1) Preprocessing: The processing starts from the stack of coregistered complex SAR images. The task of preprocessing is to estimate and remove the atmospheric phase screen (APS) of each image in the stack. The core feature of the preprocessing is *spatial difference*. It makes use of the assumption that APS is spatially slowly varying but highly uncorrelated from one image to another. Therefore, the estimates using spatially differential measurements should be "APS free." Such a method was already described in [50]. We customized it to adopt our problem [51].

The preprocessing procedures are described as follows: Images in the stack are downsampled if they are VHR. In the downsampled images stack, pixel pairs with spacing (arc) shorter than the atmospheric correlation length (typically recommended to be 2 km [52] in this paper, due to the high density of bright points, an even shorter distance of 250 m is chosen), are then selected and connected. Spatial differential measurements are calculated between the pixels in a pair. Then, we estimate the topography and motion parameters based on the single point scatterer phase model. The differential topography estimates is further integrated globally, and the topographic phase contribution is removed from each image. The remaining phase should be fairly flat. It consists of only the deformation phase, APS, and stochastic scattering phase. The unwrapped residual phase is first low-pass filtered in space to remove random noise, and high-pass filtered in time to eliminate deformation signals. The result in this step is the APS of each image on the network made up of selected pixels. After interpolation and upsampling, the APS-induced phase is removed for each image of the stack.

2) Tomographic Processing: After APS removal, tomographic processing is applied to each pixel of the stacked images aiming at the retrieval of the elevation and motion parameters of multiple scatterers inside one azimuth–range pixel. Here, the generalized time warp model with $\mathrm{M} = 2$ is used; we estimate linear and periodic seasonal motion.

Depending on the applications, different algorithms can be chosen for tomographic reconstruction.

- *PSI*: PSI is a special case of TomoSAR that attempts to separate the following phase contributions: elevation of the point, deformation parameters (e.g., deformation rate and amplitude of seasonal motion), orbit errors, and tropospheric water vapor delay. This is done by assuming the presence of only a single scatterer in the pixel. This restriction brings the big advantage of computational efficiency. It is recommended for large-scale urban monitoring.

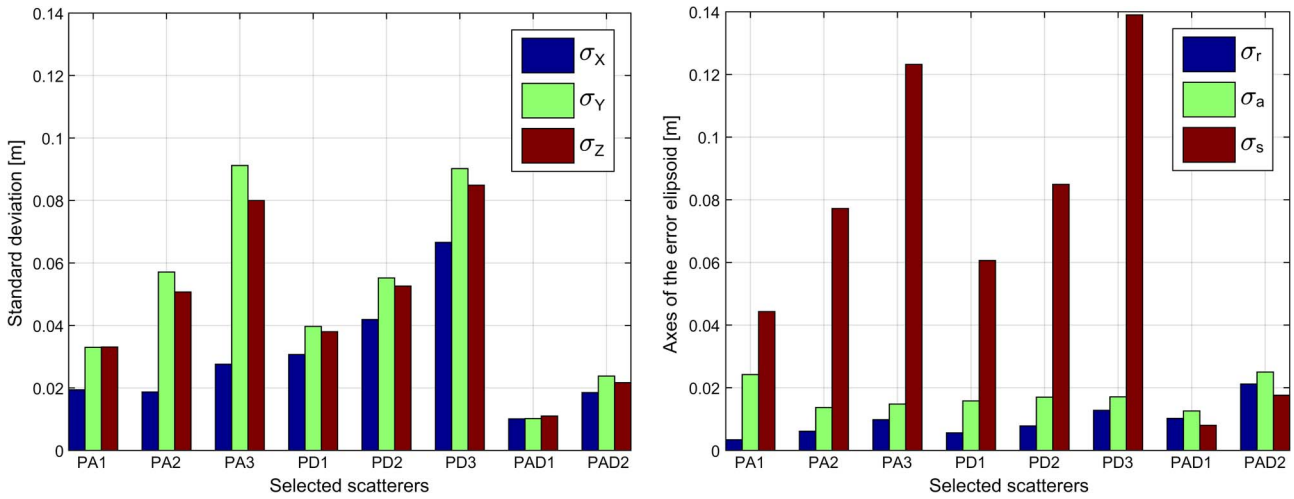

Fig. 7. Estimated coordinate stochastics for three components obtained from stereo SAR. The importance of geometry configuration on 3-D positioning is clearly seen as the scatterers localized from cross-heading tracks are more precise.

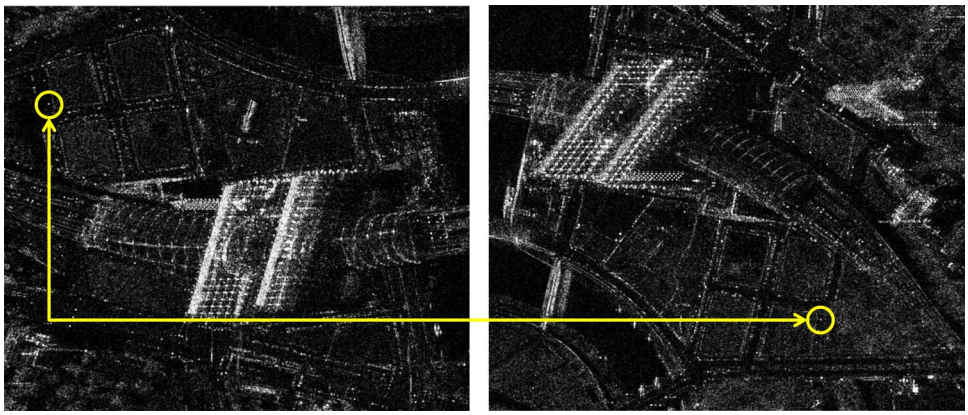

Fig. 8. Common target visible in all ascending and descending data stacks, which is selected as the reference point for the follow-on TomoSAR processing. The point can be observed as a bright dot inside the yellow circles.

- *Maximum detection (MD)*: MD stands for SVD-Wiener (linear MAP) reconstruction followed by peak detection and model order selection and final refinement of the amplitude and phase estimates [4]. This algorithm is computationally efficient and is not sensitive to irregular sampling. As a linear method, MD has almost no super-resolution capability. Taking account to its fast computation, MD is recommended if the native elevation resolution is sufficient for the application.
- *Scale-down by L_1 norm minimization, model selection, and estimation reconstruction (SL1MMER)*: The SL1MMER algorithm is proposed in [53]. It consists of three main steps: 1) a dimensionality scale down by L_1 norm minimization; 2) model selection; and 3) parameter estimation. In [24] and [54], this algorithm is demonstrated to give robust estimation with very high elevation resolution. In the relevant parameter range for TomoSAR, super-resolution factors of 1.5–25 (compared with the Rayleigh resolution unit) can be expected. SL1MMER can offer so far ultimate 4-D SAR imaging; however, it is computationally very expensive. Therefore, it is recommended for the monitoring of individual high rise buildings.
- *Integrated Approach*: Considering the high computational cost of TomoSAR, tomographic SAR inversion is integrated with PSI for operational use in [51]. With the integration of PSI, the processing is 30–50 times faster than SL1MMER alone, and still comparable results can be achieved. Thus, it gives a good compromise of the aforementioned three methods.

Since our aim is to demonstrate the framework of *geodetical* SAR tomography, the simple MD method, i.e., SVD-Wiener followed by model order selection and parameter estimation, is chosen for an efficient TomoSAR processing. Starting from SLCs, for an input data stack, the Tomo-GENESIS system retrieves the following information: number of scatterers inside each azimuth–range pixel, amplitude and phase, topography and motion parameters (e.g., linear deformation velocity and amplitude of thermal dilation induced seasonal motion) of each detected scatterer with respect to a reference point.

The final elevation estimates of two of the four data stacks using the same reference point are exemplified in Fig. 9. The elevation is color-coded. Fig. 9(a) and (b) refers to the result for beams 42 and 57, respectively. For each of the retrieved

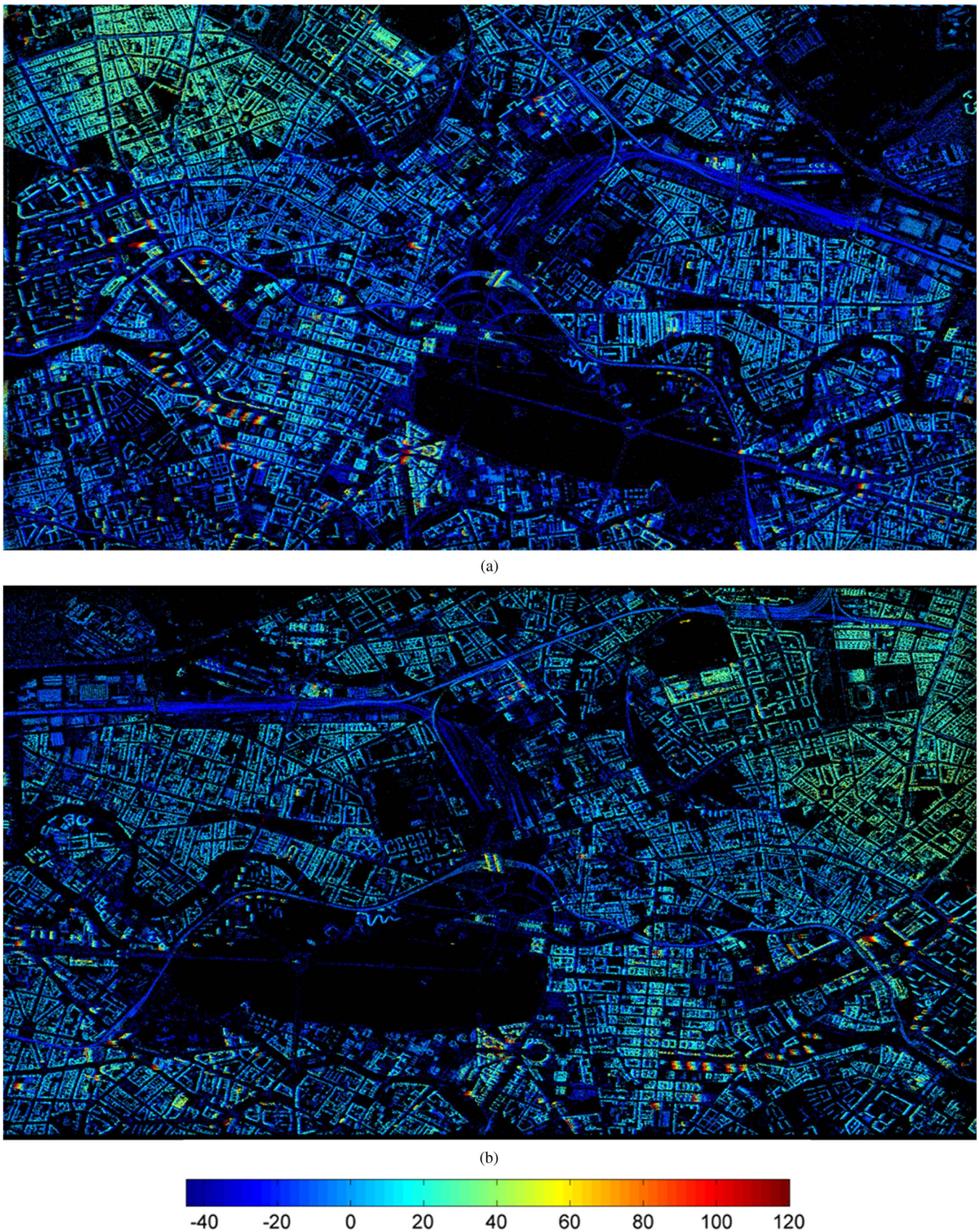

Fig. 9. TomoSAR results. Elevation estimates of two of the four stacks using the same reference point; elevation is color-coded [unit: m]. (a) Beam 42, descending. (b) Beam 57, ascending.

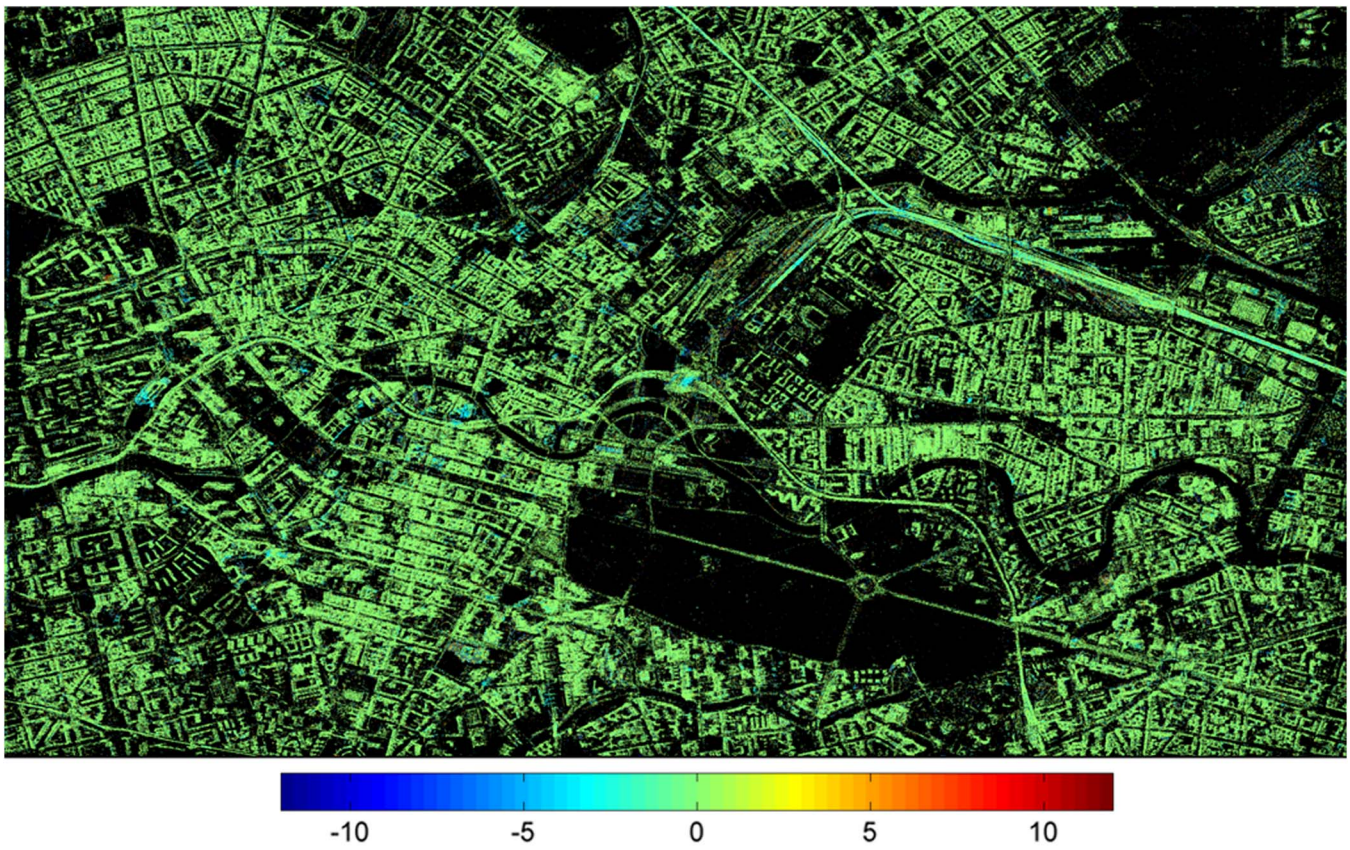

(a)

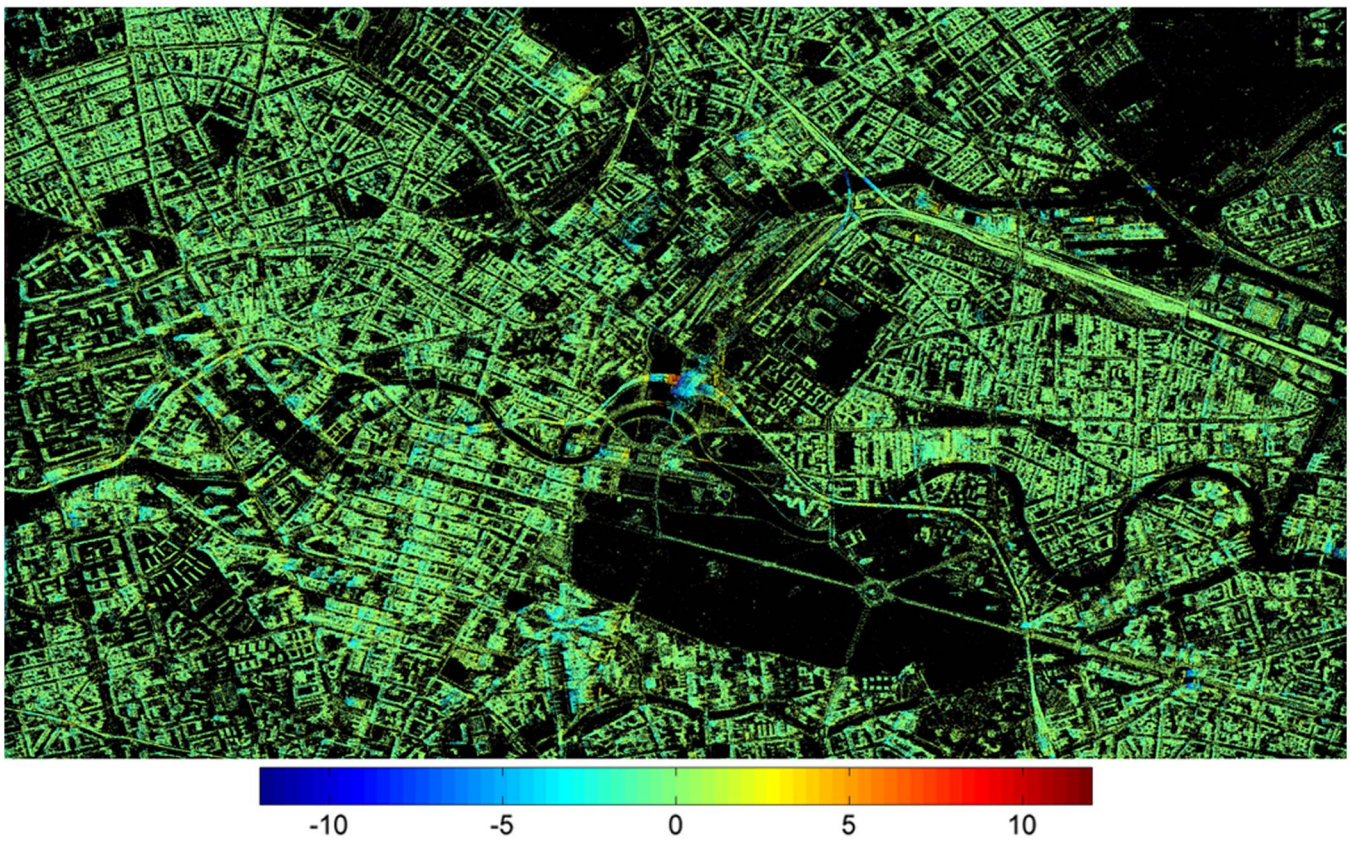

(b)

Fig. 10. TomoSAR results. Estimated LOS linear deformation rate (a) and amplitude of seasonal motion (b) of beam 42. Motion parameter is color-coded. (a) Linear deformation rate [mm/y]. (b) Amplitude of seasonal motion [mm].

scatterers/points, its undergoing amplitude of seasonal motion and linear deformation rate are also estimated.

Since, in this paper, mainly the absolute positions of these scatterers are concerned, the motion results will not be discussed further. To give the readers an impression of the estimated motion parameters, Fig. 10 shows the estimated LOS linear deformation (a) rate and (b) amplitude of seasonal motion of beam 42 as an example. It can be observed that Berlin is rather stable, i.e., there is no significant ground deformation pattern. Most of the buildings and other man-made urban infrastructures mainly undergo temperature changes and induced seasonal deformation with amplitude of up to 15 mm. Some railway sections, the buildings along them, and several buildings in construction undergo a linear subsidence with a rate of up to 8 mm/y. For a more meaningful analysis, LOS deformation estimates of different viewing angles need to be fused [55].

D. Geodetic Fusion of TomoSAR Point Clouds

The side-looking geometry of SAR sensors only allows for mapping the illuminated sides of buildings. In order to produce a shadow-free point cloud, coregistration of results from, at least, one set of cross-heading orbits is required. For PSI and TomoSAR whose estimates are relative, geocoded point clouds obtained from different acquisition geometries cannot be directly coregistered. This is mainly due to the offsets in the elevation direction that are caused by selection of reference points with unknown heights, during the processing. The coregistration task of two unstructured 3-D InSAR point clouds is referred to as point cloud fusion in the SAR community. In [42], a method for fusion of multitrack PSI results is proposed based on a least-squares matching scheme that minimizes the distances between assumed identical points of two point clouds. The method aims to estimate the offset between the identical points in the elevation direction. In [44], an alternative feature-based fusion algorithm is proposed, which is based on automatic detection and matching the so-called *L-shapes* of high rise buildings from InSAR point clouds. This method is computationally more efficient than the one introduced in [42] due to the reduced number of points in the matching step. Relevant work in the airborne research domain can be found in [56] and [57]. It is important to note that all mentioned existing methods perform the point cloud fusion *geometrically*. It can be shown that by merging the capabilities of the stereo SAR (see Section II) and TomoSAR (see Section III), it is possible to perform *geodetic* point cloud fusion.

In the framework of geodetical SAR tomography, TomoSAR processing is based on the selection of an identical reference point whose 3-D positions are retrieved by means of stereo SAR. After geocoding, it is therefore expected that the point clouds will be automatically fused without further manipulations. However, this is not true for the following reasons.

- Each point cloud is geocoded separately based on the corresponding noncorrected range and azimuth timing information. As a consequence, the geocoded coordinates of the reference point, in each stack, show offsets with respect to the reference point coordinates obtained from stereo SAR, as well as to the geocoded reference point coordinates of other stacks.
- Scatterers visible in SAR images acquired in urban environment from both ascending and descending orbits, which are assumed identical in stereo SAR processing, are often lamp posts [37]. The SAR illuminates different sides of the lamp post from ascending and descending orbits. This means the identical scatterer assumption is not fully valid. Under the assumption that these two points are identical in 3-D, the reference point coordinates obtained from stereo SAR is situated on the body between the two sides of the lamp post. The coordinate offsets of the true reference points of individual stacks and the results obtained from stereo SAR depend on the diameter of the lamp post and incidence angles of each stack.

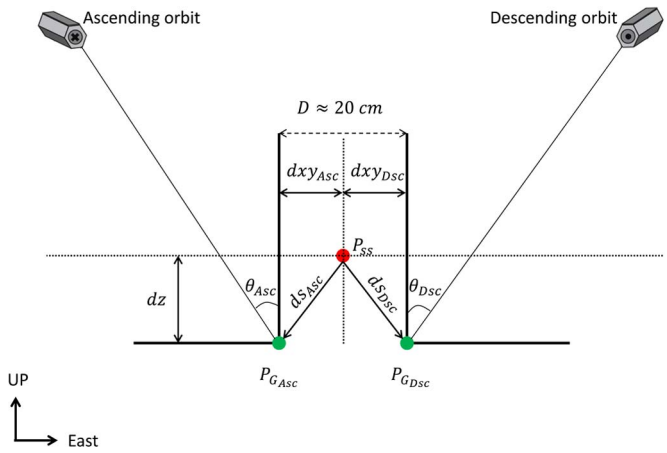

Fig. 11. Shift between the geocoded reference points in TomoSAR point clouds obtained from cross-heading geometries relevant to our specific case. The drawing is in the east-up plane while ascending and descending satellites fly perpendicular to the plane far away and toward the reader, respectively. For successful point cloud fusion, the coordinates resulted from stereo SAR $(\mathrm{P_{SS}})$ should be shifted toward the expected true position of the reference point in each ascending and descending stack $(\mathrm{P_{G_{Asc}}}, \mathrm{P_{G_{Dsc}}})$. In order to do so, the corresponding shift vector in the elevation direction $(\mathrm{ds_{Asc}}, \mathrm{ds_{Dsc}})$ should be evaluated for each stack based on the known local incidence angles $(\theta_{\mathrm{Asc}}, \theta_{\mathrm{Dsc}})$ and the heading angles of the satellites $(\alpha_{\mathrm{Asc}}, \alpha_{\mathrm{Dsc}})$.

In order to compensate for the mentioned offsets, corrections are further required. For successful fusion of TomoSAR point clouds obtained from different viewing geometries, the coordinate shifts between the geocoded coordinates of the reference point in each stack and the reference point coordinates obtained from stereo SAR should be resolved.

Fig. 11 describes the problem stated earlier related to the nonmodeled diameter of the lamp post. The drawing is depicted in the (approximately) east-up plane where it is assumed that the ascending (left) and descending (right) satellites fly away and toward the reader, respectively. The diameter of the lamp post (D) is approximately 20 cm. The red dot denotes the approximate position of the reference point whose coordinates are retrieved with the stereo SAR method $\mathbf{P}_{\mathrm{SS}}$. The two green dots indicate the true positions on which the geocoded reference points in the point clouds obtained from ascending $(\mathbf{P}_{G_{\mathrm{Asc}}})$ and the descending $(\mathbf{P}_{G_{\mathrm{Dsc}}})$ tracks should be located. In order

Fig. 12. Optical image of Federal Intelligence Building (Google Earth). The part in the red ellipse is investigated later to compare the fusion results before and after applying the coordinate corrections.

to compensate the offset between the two cross-heading point clouds, caused by the diameter of the lamp post, for each of the ascending and descending stacks, $\mathbf{P}_{\mathrm{SS}}$ should be shifted to the corresponding illuminated base of the lamp post by evaluation of the shift vectors $\mathbf{ds}_{\mathrm{Asc}}, \mathbf{ds}_{\mathrm{Dsc}}$ in the elevation direction. With the knowledge of the local incidence angle of each beam at the location of the lamp post $(\theta_{\mathrm{Asc}}, \theta_{\mathrm{Dsc}})$ and the satellites heading angles $(\alpha_{\mathrm{Asc}}, \alpha_{\mathrm{Dsc}})$, each component of the shift vectors can be calculated as follows:

$$dz = \frac{D \cdot \tan(\theta_{\mathrm{Asc}}) \cdot \tan(\theta_{\mathrm{Dsc}})}{\tan(\theta_{\mathrm{Asc}}) + \tan(\theta_{\mathrm{Dsc}})} \tag{7}$$

$$dx_{\mathrm{Asc}} = dxy_{\mathrm{Asc}} \cdot \cos(\alpha_{\mathrm{Asc}}) \tag{8}$$

$$dy_{\mathrm{Asc}} = -dxy_{\mathrm{Asc}} \cdot \sin(\alpha_{\mathrm{Asc}}) \tag{9}$$

$$dx_{\mathrm{Dsc}} = dxy_{\mathrm{Dsc}} \cdot \cos(\alpha_{\mathrm{Dsc}}) \tag{10}$$

$$dy_{\mathrm{Dsc}} = -dxy_{\mathrm{Dsc}} \cdot \sin(\alpha_{\mathrm{Dsc}}). \tag{11}$$

$dxy_{\mathrm{Asc}} = dz \cdot \cot(\theta_{\mathrm{Asc}})$ and $dxy_{\mathrm{Dsc}} = dz \cdot \cot(\theta_{\mathrm{Dsc}})$. Shift in the upward direction (dz) is equal for all the stacks and therefore can be evaluated using a least squares adjustment based on different combinations of the ascending and descending tracks. Afterward, the individual horizontal shifts $(dxy_{\mathrm{Asc}}, dxy_{\mathrm{Dsc}})$ are calculated for each stack, and with the known azimuth angles, they are projected into the east and north directions $(dx_{\mathrm{Asc}}, dy_{\mathrm{Asc}}, dx_{\mathrm{Dsc}}, dy_{\mathrm{Dsc}})$. The shift vectors thus are formed as

$$\mathbf{d}s_{\mathrm{Asc}} = [dx_{\mathrm{Asc}}, dy_{\mathrm{Asc}}, dz_{\mathrm{Asc}}]^T \tag{12}$$

$$\mathbf{d}s_{\mathrm{Dsc}} = [dx_{\mathrm{Dsc}}, dy_{\mathrm{Dsc}}, dz_{\mathrm{Dsc}}]^T. \tag{13}$$

Subsequently, $\mathbf{P}_{\mathrm{SS}}$ is shifted to the position of $\mathbf{P}_{G_{\mathrm{Asc}}}$ or $\mathbf{P}_{G_{\mathrm{Dsc}}}$ that is dependent on the acquisition geometry of the stack

$$\mathbf{P}_{G_{\mathrm{Asc}}} = \mathbf{P}_{\mathrm{SS}} - \mathbf{d}s_{\mathrm{Asc}} \tag{14}$$

$$\mathbf{P}_{G_{\mathrm{Dsc}}} = \mathbf{P}_{\mathrm{SS}} - \mathbf{d}s_{\mathrm{Dsc}}. \tag{15}$$

The remaining errors of the geocoding is compensated by evaluating the difference between the geocoded reference point coordinates of each stack and the corresponding $\mathbf{P}_{G_{\mathrm{Asc}}}$ or $\mathbf{P}_{G_{\mathrm{Dsc}}}$. Finally, for each stack, the unique difference vector is added to the coordinates of all the scatterers to produce four absolutely localized corrected point clouds.

Compensation for the coordinate shifts between the geocoded reference points and true position of the stereo SAR results allows for seamless geodetic fusion of TomoSAR point clouds. These corrections have been applied to each point cloud separately. To confirm that the corrections are necessary, a small test site including the Federal Intelligence Service (BND) building in Berlin is chosen to compare the fusion results before and after applying the coordinate corrections. Fig. 12 shows the optical image of the building. The red ellipse marks the building section that is investigated in Fig. 13.

In Fig. 13, the results from the ascending stacks are visualized in blue, and the descending point clouds are shown in red. In the noncorrected fusion (left), the black arrow represents the shift available between the same heading tracks. Moreover, the black ellipse highlights that the result from descending stacks (red) does not match with the building fraction captured from ascending stacks (blue). The right figure illustrates the fused point clouds by applying all aforementioned corrections. The good match of all four point clouds confirms the effectiveness of the proposed fusion strategy.

Fig. 14 illustrates the fusion of two ascending and two descending absolute TomoSAR point clouds in 2-D over the city of Berlin. The coordinates are expressed in Universal Transverse Mercator (UTM) coordinate system. It is seen that the point clouds are reasonably overlaid on each other after applying the corrections. This part is finalized by 2-D and 3-D visualizations of the fused point cloud of the central urban area of Berlin illustrated in Fig. 15. The absolute point clouds are plotted in the UTM coordinate system, and the height of each scatterer is color-coded with respect to the WGS84 ellipsoid.

The coverage of the test site is approximately 10 km $\times$ 5 km and the number of captured absolute positioned scatterers is 63 million. It is clearly seen that the fusion of TomoSAR point clouds obtained from different geometries allows for highly detailed 3-D mapping of the city. It is worth to mention that the aforementioned point density is obtained using the computationally efficient MD estimator, processing the same data sets using more expensive algorithms, e.g., SL1MMER, will even lead to a significantly higher point density [54]. This aspect is however outside the scope of this paper.

V. Localization Accuracy Analysis of the Fused TomoSAR Point Cloud

The localization accuracy of the fused TomoSAR point cloud is assessed by comparing the results with an accurate DSM calculated from a point cloud obtained from aerial laser scanning

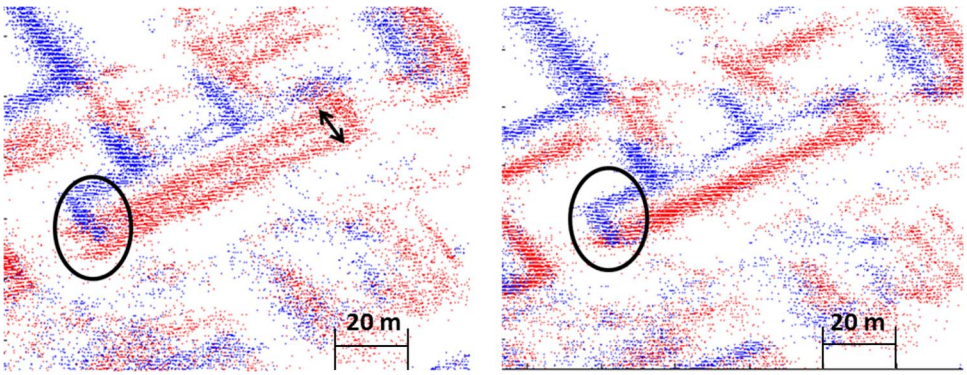

Fig. 13. Comparison between the fusion results before (left) and after (right) applying the reference point coordinate correction. The result from the ascending stacks is visualized in blue, and the descending point clouds are shown in red. The noncorrected fusion (left) includes certain offsets between the results from same-heading tracks (the black arrow) and wrong intersection of different building fractions captured from cross-heading tracks (the back ellipse).

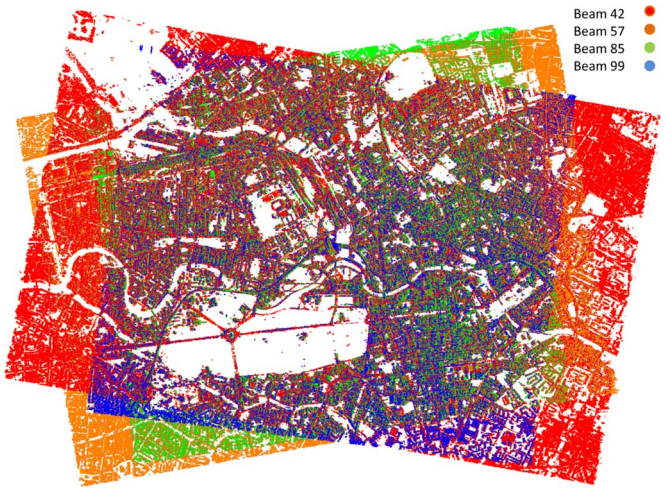

Fig. 14. Fusion result of two ascending and two descending tracks over the city of Berlin. The point clouds are absolutely localized after correcting the geocoded coordinates of the reference point and are geodetically fused.

characterized with a large number of data points and high absolute geolocalization accuracy on the order of 10 cm. This allows for a quantitative analysis on the positioning accuracy of the TomoSAR point cloud.

To check the overall accuracy of the point cloud, Fig. 16(a) shows the fused TomoSAR point cloud of a small area of Berlin overplotted onto the corresponding area in LiDAR DSM. The heights of the scatterers are color-coded with blue to red values indicating lower to higher heights. The DSM is plotted in gray for better visualization purposes. The good fit of the TomoSAR point cloud on the DSM is visually observable. For a closer speculation, a cross section through the buildings, marked with a white rectangle in Fig. 16(a), is visualized in Fig. 16(b). The figure shows a slice in the xz plane with the height values color coded. In order to validate the results illustrated in Fig. 16, the accuracy analysis is carried out for horizontal and vertical directions separately as reported in the following.

A. Horizontal Accuracy Analysis

The optimum way to assess the accuracy of the fused TomoSAR point cloud is a point-wise comparison with respect to the LiDAR point cloud. However, this is not feasible as LiDAR sensors map the surface with a nadir looking angle, whereas SAR sensors capture the scene from a side-looking geometry. The difference in acquisition geometry leads to different mapping of the same object and therefore complicates the comparison.

In this paper, the horizontal assessment is carried out by evaluating the mean façade points from the TomoSAR point cloud with respect to the extracted corresponding façade line from the LiDAR DSM.

- Building façades from the LiDAR DSM are estimated as follows: Based on the top view extent of the building, an area is cropped, which contains the desired building fraction. Centered on each point inside the cropped scene, a vertical cylinder with the radius of 2 m is considered. Inside the cylinder, the height variance is calculated. Points with height variances higher than a threshold are labeled as façade points. The building façade surface is assumed vertical. Therefore, at the final step, the footprint of the façade in 2-D, i.e., on the ground plane, is estimated by fitting a line to the façade points using reweighted least squares with a bisquare weighting function.
- For the TomoSAR point cloud, points belonging to a specific façade are extracted using the algorithms proposed in [58] and [59]: First, the scatterer density in the horizontal plane is estimated in adaptive windows varying dependent on the orientation of the façades. Based on the estimated point density and local normal directions, points belonging to individual building façades are extracted.

The perpendicular distance between the façade points extracted from TomoSAR point clouds and the corresponding façade lines estimated from LiDAR DSM is calculated. The mean value of the deviations is regarded as the horizontal bias between the TomoSAR point cloud and the LiDAR DSM.

B. Vertical Accuracy Analysis

The vertical accuracy is analyzed by comparing identical flat grounds mapped in LiDAR DSM and in the fused TomoSAR

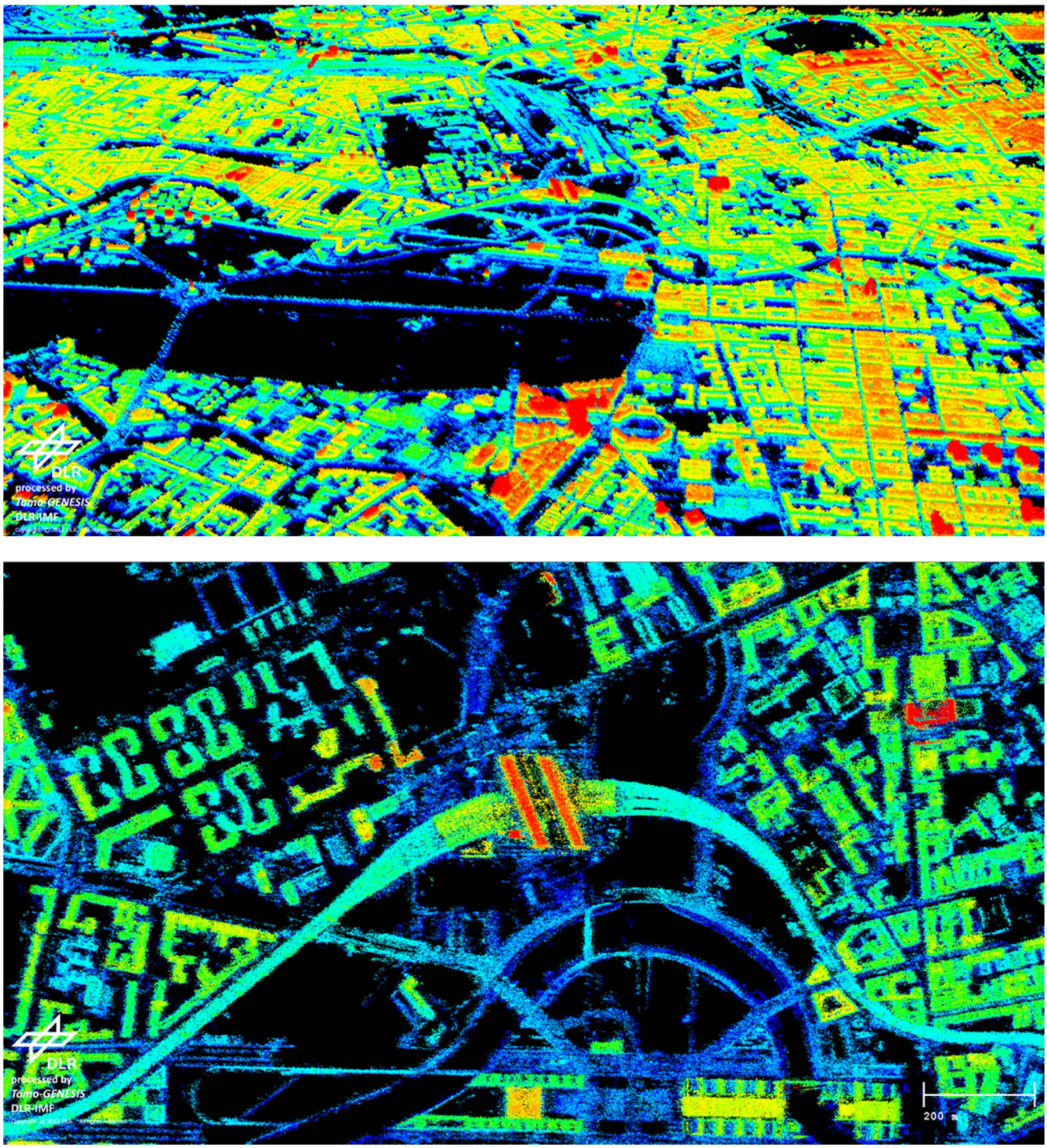

Fig. 15. Three-dimensional absolutely positioned TomoSAR point clouds in 3-D (top) and 2-D (bottom). The absolute height values are color-coded and range between 70 m to 110 m. Clearly, the fusion of multitrack point clouds allow for a very detailed representation of the city where most of the structures can be easily recognized.

point cloud. An identical patch is selected from both the TomoSAR point cloud and the reference surface. Inside the patch, the height deviation of scatterers from the TomoSAR point cloud with respect to the flat scene in the LiDAR DSM is evaluated by calculating the root mean square error.

C. Test Sites and Discussion

Different test sites from Berlin are chosen to validate the positioning accuracy of the fused TomoSAR point cloud. For horizontal analysis, two different buildings are selected, and for each of them, the extracted façade in the LiDAR DSM is

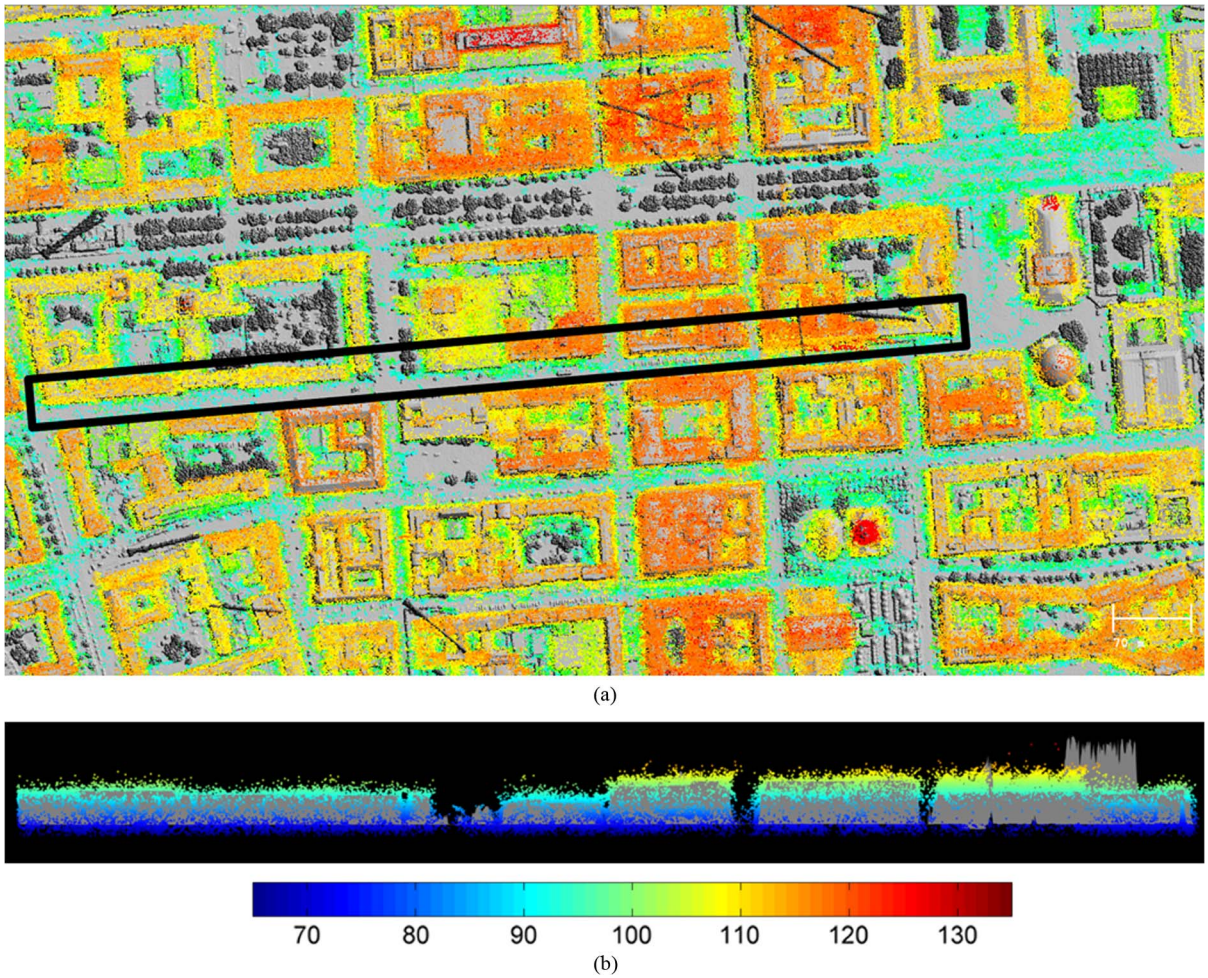

Fig. 16. (a) Fused TomoSAR point cloud overplotted onto the reference DSM. The DSM is plotted in gray for better visualization purposes. The height of the TomoSAR point cloud is color coded. It is seen that the scatterers are fitted to the corresponding building parts on the DSM as no large deviations are visible from the plot. The cross section in the xz plane visualized in (b) confirms the mentioned statement. [unit: meters].

compared with the detected façade points in the TomoSAR point cloud. Fig. 17 shows the findings of the first test site including a high-rise building in Postdamer Platz located at a distance of approximately 2 km from the reference point. Fig. 17(a) shows the optical image of the area where the investigated façade is marked with a white rectangle. Fig. 17(b) and (c) shows the mapped area in the LiDAR DSM and the TomoSAR point cloud in the UTM coordinate system with the facade distinguished with a white rectangle and a black rectangle, respectively. Façade points from the LiDAR DSM are extracted based on a threshold of 20 m on the height standard deviation values estimated in a vertical cylinder with the radius of 2 m around each point. The façade footprint, i.e., a line on the ground plane, is then the estimated. Fig. 17(d) shows the LiDAR façade points, color-coded based on the height variance values, and the estimated façade line in red. Façade points in the TomoSAR point cloud are approximated by applying a threshold of 13 points/m^2 on the scatterer density estimates. Moreover, the TomoSAR point cloud is clipped within height values of 80 to 160 m. The latter is carried out based on the information from the LiDAR DSM, which shows that the façade points are most likely located within the mentioned height interval. The result is shown in Fig. 17(e), where the detected TomoSAR façade points are color-coded based on the scatterer density estimates and are plotted along with the estimated façade line from the LiDAR DSM. Eventually, Fig. 17(f) shows the histogram of the perpendicular distances between the TomoSAR façade points and the fitted LiDAR façade line. The mean value of the distances implies the bias between the TomoSAR point cloud and the LiDAR DSM for this specific test site, which is equal to -0.184 m. The standard deviation hints the estimation accuracy of TomoSAR, which is equal to 1.17 m. It matches well with the meter-order elevation estimatio accuracy calculated from the derived Cramér–Rao lower bound [31].

For vertical accuracy analysis, several test sites are selected. The important criterion in the selection of the test sites is that they should be absolutely located on flat ground. Experiences show that the deviations within a couple of meters exist between the TomoSAR point cloud and the LiDAR DSM. This corresponds to: 1) the meter-level elevation estimation accuracy of repeat–pass InSAR, such as TomoSAR; and 2) the fact the roof points or ground points selected for evaluation are very unlikely being precisely located on flat surfaces as desired.

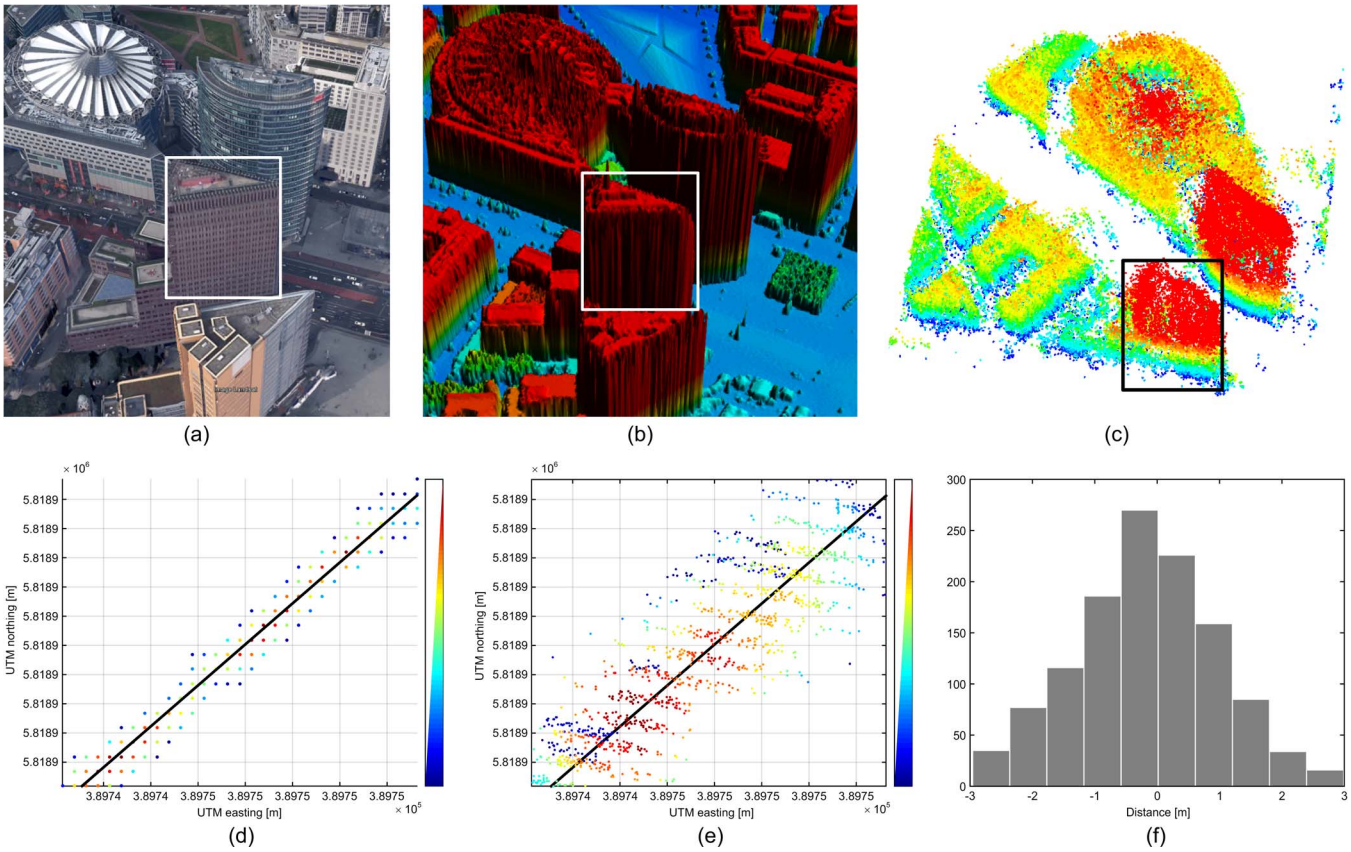

Fig. 17. First test site for the horizontal accuracy analysis of the TomoSAR point cloud. The investigated façade is marked with white rectangles. (a) Optical image of Postdamer Platz (Google Earth). (b) Corresponding LiDAR DSM. (c) Corresponding TomoSAR point cloud. d) Detected façade points from the LiDAR DSM and the estimated façade line in UTM projection. The façade points are color-coded based on the height variance values and the façade line is expressed in black. (e) Detected façade points from the TomoSAR point cloud, color-coded based on the scatterer density values, and the façade line fitted to LIDAR DSM drawn in black. (f) Histogram of differences between TomoSAR façade points and the façade line in LiDAR DSM. The histogram is centered on −0.184 m, which hints the achieved absolute positioning accuracy.

VI. Conclusion

In this paper, we have proposed the "geodetic TomoSAR" framework that fuses SAR image geodesy and SAR tomography to obtain *absolute* 3-D positions of a large amount of natural scatterers. An absolute 3-D TomoSAR point cloud with 63 million points covering an area of 10 km × 5 km over the city of Berlin is presented. Compared with a high-precision LiDAR DEM, the absolute positioning accuracy of the proposed approach reaches 20 cm. It demonstrates the applicability of the proposed approach. Future work concentrates on: 1) automatic identification of common scattering objects appearing in SAR images obtained from different geometries, e.g., by exploring the regular pattern attributed to building façades (for same heading orbits) or street lamps (for cross heading orbits); and 2) investigation on absolute deformation estimates for large area, e.g., by cooperating GPS measurements.

Acknowledgment

The authors gratefully acknowledge the Gauss Centre for Supercomputing e.V for providing computing time at the GCS Supercomputer SuperMUC at the Leibniz Supercomputing Centre.

References

[1] G. Fornaro, F. Serafino, and F. Soldovieri, "Three-dimensional focusing with multipass SAR data," *IEEE Trans. Geosci. Remote Sens.*, vol. 41, no. 3, pp. 507–517, Mar. 2003.

[2] F. Lombardini, "Differential tomography: A new framework for SAR interferometry," *IEEE Trans. Geosci. Remote Sens.*, vol. 43, no. 1, pp. 37–44, Jan. 2005.

[3] G. Fornaro, D. Reale, and F. Serafino, "Four-dimensional SAR imaging for height estimation and monitoring of single and double scatterers," *IEEE Trans. Geosci. Remote Sens.*, vol. 47, no. 1, pp. 224–237, Jan. 2009.

[4] X. X. Zhu and R. Bamler, "Very high resolution spaceborne SAR tomography in urban environment," *IEEE Trans. Geosci. Remote Sens.*, vol. 48, no. 12, pp. 4296–4308, Dec. 2010.

[5] X. X. Zhu and R. Bamler, "Let's do the time warp: Multicomponent nonlinear motion estimation in differential SAR tomography," *IEEE Geosci. Remote Sens. Lett.*, vol. 8, no. 4, pp. 735–739, Jul. 2011.

[6] Y. Wang, X. X. Zhu, Y. Shi, and R. Bamler, "Operational TomoSAR processing using terrasar-X high resolution spotlight stacks from multiple view angles," in *Proc. IEEE IGARSS*, 2012, pp. 7047–7050.

[7] P. Ma, H. Lin, H. Lan, and F. Chen, "On the performance of reweighted minimization for tomographic SAR imaging," *IEEE Geosci. Remote Sens. Lett.*, vol. 12, no. 4, pp. 895–899, Apr. 2015.

[8] L. Wei, T. Balz, L. Zhang, and M. Liao, "A novel fast approach for SAR tomography: Two-step iterative shrinkage/thresholding," *IEEE Geosci. Remote Sens. Lett.*, vol. 12, no. 6, pp. 1377–1381, Jun. 2015.

[9] O. Frey, I. Hajnsek, U. Wegmuller, and C. L. Werner, "SAR tomography based 3-D point cloud extraction of point-like scatterers in urban areas," in *Proc. IEEE IGARSS*, 2014, pp. 1313–1316.

[10] A. Ferretti, C. Prati, and F. Rocca, "Permanent scatterers in SAR interferometry," *IEEE Trans. Geosci. Remote Sens.*, vol. 39, no. 1, pp. 8–20, Jan. 2001.

[11] N. Adam, B. Kampes, M. Eineder, J. Worawattanamateekul, and M. Kircher, "The development of a scientific permanent scatterer system," in *Proc. ISPRS Workshop High Resolution Mapping Space*, *Hannover, Germany*, 2003, vol. 2003, p. 6.

[12] B. M. Kampes, *Radar Interferometry—Persistent Scatterer Technique*, vol. 12. Dordrecht, The Netherlands: Springer-Verlag, 2006.

[13] S. Gernhardt, N. Adam, M. Eineder, and R. Bamler, "Potential of very high resolution SAR for persistent scatterer interferometry in urban areas," *Ann. GIS*, vol. 2, no. 16, pp. 103–111, Sep. 2010.

[14] Z. Wang, D. Perissin, and H. Lin, "Subway tunnels identification through Cosmo-SkyMed PSInSAR analysis in Shanghai," in *Proc. IEEE IGARSS*, 2011, pp. 1267–1270.

[15] P. Berardino, G. Fornaro, R. Lanari, and E. Sansosti, "A new algorithm for surface deformation monitoring based on small baseline differential SAR interferograms," *IEEE Trans. Geosci. Remote Sens.*, vol. 40, no. 11, pp. 2375–2383, Nov. 2002.

[16] R. Lanari *et al.*, "A small-baseline approach for investigating deformations on full-resolution differential SAR interferograms," *IEEE Trans. Geosci. Remote Sens.*, vol. 42, no. 7, pp. 1377–1386, Jul. 2004.

[17] K. Goel and N. Adam, "An advanced algorithm for deformation estimation in non-urban areas," *ISPRS J. Photogramm. Remote Sens.*, vol. 73, pp. 100–110, Sep. 2012.

[18] A. Ferretti *et al.*, "A new algorithm for processing interferometric data-stacks: SqueeSAR," *IEEE Trans. Geosci. Remote Sens.*, vol. 49, no. 9, pp. 3460–3470, Sep. 2011.

[19] Y. Wang, X. X. Zhu, and R. Bamler, "Retrieval of phase history parameters from distributed scatterers in urban areas using very high resolution SAR data," *ISPRS J. Photogramm. Remote Sens.*, vol. 73, pp. 89–99, Sep. 2012.

[20] Y. Wang, X. X. Zhu, and R. Bamler, "Robust covariance matrix estimation with application to volcano monitoring using SAR image stacks," in *Proc. EUSAR*, 2014, pp. 1–4.

[21] G. Fornaro, A. Pauciullo, D. Reale, and S. Verde, "Improving SAR tomography urban area imaging and monitoring with CAESAR," in *Proc. EUSAR*, 2014, pp. 1–4.

[22] X. X. Zhu, N. Adam, and R. Bamler, "First demonstration of spaceborne high resolution SAR tomography in urban environment using TerraSAR-X data," in *Proc. CEOS SAR Workshop*, Oberpfaffenhofen, Germany, 2008, pp. 1–8.

[23] D. Reale, G. Fornaro, A. Pauciullo, X. Zhu, and R. Bamler, "Tomographic imaging and monitoring of buildings with very high resolution SAR data," *IEEE Geosci. Remote Sens. Lett.*, vol. 8, no. 4, pp. 661–665, Jul. 2011.

[24] X. Zhu and R. Bamler, "Demonstration of super-resolution for tomographic SAR imaging in urban environment," *IEEE Trans. Geosci. Remote Sens.*, vol. 50, no. 8, pp. 3150–3157, Aug. 2012.

[25] R. Bamler, M. Eineder, N. Adam, X. Zhu, and S. Gernhardt, "Interferometric potential of high resolution spaceborne SAR," *Photogramm.—Fernerkund.—Geoinf.*, vol. 2009, no. 5, pp. 407–419, Nov. 2009.

[26] G. Fornaro, F. Lombardini, A. Pauciullo, D. Reale, and F. Viviani, "Tomographic processing of interferometric SAR data: Developments, applications, and future research perspectives," *IEEE Signal Process. Mag.*, vol. 31, no. 4, pp. 41–50, Jul. 2014.

[27] X. X. Zhu and R. Bamler, "Superresolving SAR tomography for multidimensional imaging of urban areas: Compressive sensing-based TomoSAR inversion," *IEEE Signal Process. Mag.*, vol. 31, no. 4, pp. 51–58, Jul. 2014.

[28] M. Eineder, C. Minet, P. Steigenberger, X. Cong, and T. Fritz, "Imaging geodesy—Toward centimeter-level ranging accuracy with TerraSAR-X," *IEEE Trans. Geosci. Remote Sens.*, vol. 49, no. 2, pp. 661–671, Feb. 2011.

[29] X. Cong, U. Balss, M. Eineder, and T. Fritz, "Imaging geodesy—Centimeter-level ranging accuracy with TerraSAR-X: An update," *IEEE Geosci. Remote Sens. Lett.*, vol. 9, no. 5, pp. 948–952, Sep. 2012.

[30] F. W. Leberl, *Radargrammetric Image Processing*. Rijeka, Croatia: InTech, 1990.

[31] X. X. Zhu and R. Bamler, "Super-resolution power and robustness of compressive sensing for spectral estimation with application to spaceborne tomographic SAR," *IEEE Trans. Geosci. Remote Sens.*, vol. 50, no. 1, pp. 247–258, Jan. 2012.

[32] U. Balss *et al.*, "Precise measurements on the absolute localization accuracy of TerraSAR-X on the base of far-distributed test sites," in *Proc. EUSAR*, 2014, pp. 1–4.

[33] H. Breit, E. Börner, J. Mittermayer, J. Holzner, and M. Eineder, "The TerraSAR-X multi-mode SAR processor—Algorithms and design," in *Proc. EUSAR*, 2004, pp. 501–503.

[34] G. Petit and B. Luzum, *IERS Conventions (2010)*. Frankfurt, Germany: Verlag des Bundesamts für Kartographie und Geodäsie, 2010.

[35] B. Hofmann-Wellenhof, H. Lichtenegger, and E. Wasle, *GNSS—Global Navigation Satellite Systems: GPS, GLONASS, Galileo, and More*. Wein, Austria: Springer-Verlag, 2007.

[36] P. S. Mahapatra, S. Samiei-Esfahany, H. van der Marel, and R. F. Hanssen, "On the use of transponders as coherent radar targets for SAR Interferometry," *IEEE Trans. Geosci. Remote Sens.*, vol. 52, no. 3, pp. 1869–1878, Mar. 2014.

[37] C. Gisinger *et al.*, "Precise three-dimensional stereo localization of corner reflectors and persistent scatterers with TerraSAR-X," *IEEE Trans. Geosci. Remote Sens.*, vol. 53, no. 4, pp. 1782–1802, Apr. 2015.

[38] I. G. Cumming and F. H. Wong, *Digital Processing of Synthetic Aperture Radar Data: Algorithms and Implementation*, Auflage: Har/Cdr. Boston, MA, USA: Artech House, 2005.

[39] T. Fritz *et al.*, "TerraSAR-X Ground Segment Level 1b Product Format Specification." TX-GS-DD-3307, v1.3, 2007.

[40] A. Reigber and A. Moreira, "First demonstration of airborne SAR tomography using multibaseline L-band data," *IEEE Trans. Geosci. Remote Sens.*, vol. 38, no. 5, pp. 2142–2152, Sep. 2000.

[41] E. Aguilera, M. Nannini, and A. Reigber, "Multi-signal compressed sensing for polarimetric SAR tomography," in *Proc. IEEE IGARSS*, 2011, pp. 1369–1372.

[42] S. Gernhardt, X. Cong, M. Eineder, S. Hinz, and R. Bamler, "Geometrical fusion of multitrack PS point clouds," *IEEE Geosci. Remote Sens. Lett.*, vol. 9, no. 1, pp. 38–42, Jan. 2012.

[43] M. Schmitt, O. Maksymiuk, C. Magnard, and U. Stilla, "Radargrammetric registration of airborne multi-aspect SAR data of urban areas," *ISPRS J. Photogramm. Remote Sens.*, vol. 86, pp. 11–20, Dec. 2013.

[44] Y. Wang and X. X. Zhu, "Feature-Based Fusion of TomoSAR Point Clouds from Multiview TerraSAR-X Data Stacks," presented at the Geoscience and Remote Sensing Symposium (IGARSS), 2013 IEEE International, 2013, pp. 85–88.

[45] D. G. Lowe, "Object Recognition From Local Scale-Invariant Features," in *Proc. ICCV*, 1999, vol. 2, pp. 1150–1157.

[46] B. D. Lucas and T. Kanade, "An iterative image registration technique with an application to stereo vision," in *Proc. 7th Int. Joint Conf. Artif. Intell.*, San Francisco, CA, USA, 1981, vol. 2, pp. 674–679.

[47] F. Dellinger, J. Delon, Y. Gousseau, J. Michel, and F. Tupin, "SAR-SIFT: A SIFT-like algorithm for applications on SAR images," in *Proc. IEEE IGARSS*, 2012, pp. 3478–3481.

[48] X. Zhu, "Very high resolution tomographic SAR inversion for urban infrastructure monitoring: A sparse and nonlinear tour," Ph.D. dissertation, Deutsche Geodätische Kommission, Munich, Germany, 2011.

[49] X. Zhu, Y. Wang, S. Gernhardt, and R. Bamler, "Tomo-GENESIS: DLR's tomographic SAR processing system," in *Proc. JURSE*, 2013, pp. 159–162.

[50] G. Fornaro, A. Pauciullo, and F. Serafino, "Deformation monitoring over large areas with multipass differential SAR interferometry: A new approach based on the use of spatial differences," *Int. J. Remote Sens.*, vol. 30, no. 6, pp. 1455–1478, Mar. 2009.

[51] Y. Wang, X. Zhu, and R. Bamler, "An efficient tomographic inversion approach for urban mapping using meter resolution SAR image stacks," *IEEE Geosci. Remote Sens. Lett.*, vol. 11, no. 7, pp. 1–5, Jul. 2014.

[52] R. F. Hanssen, *Radar Interferometry: Data Interpretation and Error Analysis*. Dordrecht, The Netherlands: Springer-Verlag, 2001.

[53] X. Zhu and R. Bamler, "Tomographic SAR inversion by L1-norm regularization—The compressive sensing approach," *IEEE Trans. Geosci. Remote Sens.*, vol. 48, no. 10, pp. 3839–3846, Oct. 2010.

[54] X. X. Zhu and R. Bamler, "Super-Resolution of Sparse Reconstruction for Tomographic SAR Imaging—Demonstration with Real Data," in *Proc. 9th EUSAR*, 2012, pp. 215–218.

[55] S. Gernhardt and R. Bamler, "Deformation monitoring of single buildings using meter-resolution SAR data in PSI," *ISPRS J. Photogramm. Remote Sens.*, vol. 73, pp. 68–79, Sep. 2012.
[56] M. Schmitt, "Reconstruction of urban surface models from multi-aspect and multi-baseline interferometric SAR," Ph.D. dissertation, Technische Univ. München, München, Germany, 2014.
[57] M. Schmitt, "Three-dimensional reconstruction of urban areas by multi-aspect TomoSAR data fusion," in *Proc. Joint Urban Remote Sens. Event*, Lausanne, Switzerland, 2015, (On CD).
[58] X. Zhu and M. Shahzad, "Façade reconstruction using multiview spaceborne TomoSAR point clouds," *IEEE Trans. Geosci. Remote Sens.*, vol. 52, no. 6, pp. 3541–3552, Jun. 2014.
[59] M. Shahzad and X. X. Zhu, "Robust reconstruction of building facades for large areas using spaceborne TomoSAR point clouds," *IEEE Trans. Geosci. Remote Sens.*, vol. 53, no. 2, pp. 752–769, Feb. 2015.

Xiao Xiang Zhu (S'10–M'12–SM'14) received the Bachelor's degree in space engineering from the National University of Defense Technology, Changsha, China, in 2006 and the M.Sc. and Dr.-Ing. degrees and the Habilitation in signal processing from Technische Universität München (TUM), Munich, Germany, in 2008, 2011, and 2013, respectively.

In 2009, she was a Guest Scientist or a Visiting Professor with the Italian National Research Council (CNR-IREA), Naples, Italy; in 2014, with Fudan University, Shanghai, China; and in 2015, with the University of Tokyo, Tokyo, Japan. Since 2011, she has been a Scientist with the Remote Sensing Technology Institute, German Aerospace Center, Wessling, Germany, where she is currently the Head of the Team Signal Analysis. Since 2013, she has been a Helmholtz Young Investigator Group Leader and appointed as TUM Junior Fellow. In 2015, she has been appointed as the Professor for Signal Processing for Earth Observation at TUM. Her main research interests include advanced InSAR techniques such as high-dimensional tomographic SAR imaging and SqueeSAR, computer vision in remote sensing including object reconstruction and multidimensional data visualization, and modern signal processing, including innovative algorithms such as compressive sensing and sparse reconstruction, with applications in the field of remote sensing such as multi/hyperspectral image analysis.

Sina Montazeri received the Bachelor's degree in geodesy and surveying engineering from the University of Isfahan, Isfahan, Iran and the Master's degree in geomatics from the Delft University of Technology, Delft, The Netherlands in 2011 and 2014, respectively. He is currently working toward the Ph.D. degree with the Remote Sensing Technology Institute, German Aerospace Center (DLR), Wessling, Germany.

From April 2013 to May 2014, he was a Part-Time Research Assistant with the Remote Sensing Technology Institute, DLR, working on absolute localization of point clouds obtained from SAR tomography. His research interests include, InSAR processing, image and signal processing relevant to radar imagery, parameter estimation, and geodetic InSAR.

Christoph Gisinger received the Diploma in geodesy from Technische Universität Graz, Graz, Austria, and the M.Sc. degree in Earth-oriented space science and technologies from Technische Universität München, Munich, Germany. He is currently toward the Ph.D. degree in joint processing of SAR and global navigation satellite systems to retrieve geophysical signals at the Technische Universität München.

He is currently the Chair of the Institute for Astronomical and Physical Geodesy, Technische Universität München. His research interests include stereo SAR, correction modeling for absolute SAR observations, and radargrammetric image processing with focus on fusing SAR with geodetic observations to measure deformations.

Ramon F. Hanssen (ME'04–SM'15) received the M.Sc. degree in geodetic engineering and the Ph.D. degree (*cum laude*) from the Delft University of Technology, Delft, The Netherlands, in 1993 and 2001, respectively.

He was with the International Institute for Aerospace Survey and Earth Science (ITC), Enschede, The Netherlands; the University of Stuttgart, Stuttgart, Germany; and the German Aerospace Center (DLR), Wessling, Germany. He was a Fulbright Fellow at Stanford University, Stanford, CA, USA. He was also with Scripps Institution of Oceanography, La Jolla, CA, working in the field of microwave remote sensing, radar interferometry, signal processing, and geophysical application development. Since 2008, he has been an Antoni van Leeuwenhoek Professor in Earth observation with the Delft University of Technology and has been leading the Department of Geoscience and Remote Sensing since 2011. He is the author of a textbook on radar interferometry.

Richard Bamler (M'95–SM'00–F'05) received the Diploma in Electrical engineering, the Doctor of Engineering degree, and the Habilitation in signal and systems theory from the Technische Universität München (TUM), Munich, Germany, in 1980, 1986, and 1988, respectively.

From 1981 to 1989, He worked at TUM on optical signal processing, holography, wave propagation, and tomography. Since 1989, he has been with the German Aerospace Center (DLR), Wessling, Germany, where he is currently the Director of the Remote Sensing Technology Institute. In early 1994, he was a Visiting Scientist with the Jet Propulsion Laboratory, in preparation of the SIC-C/X-SAR missions. In 1996, he was a Guest Professor with the University of Innsbruck, Innsbruck, Austria. Since 2003, he has been a Full Professor in remote sensing technology at the TUM as a double appointment with his DLR position. His teaching activities include university lectures and courses on signal processing, estimation theory, and SAR. He, as well as his team and institute, has been working on SAR and optical remote sensing, image analysis and understanding, stereo reconstruction, computer vision, ocean color, passive and active atmospheric sounding, and laboratory spectrometry. They were and are responsible for the development of the operational processors for SIR-C/X-SAR, SRTM, TerraSAR-X, TanDEM-X, Tandem-L, ERS-2/GOME, ENVISAT/SCIAMACHY, MetOp/GOME-2, Sentinel 5p, EnMAP, etc. His research interests include algorithms for optimum information extraction from remote sensing data with emphasis on SAR. This involves new estimation algorithms, such as sparse reconstruction and compressive sensing. He has devised several high-precision algorithms for monostatic and bistatic SAR processing, SAR calibration and product validation, ground moving target identification for traffic monitoring, SAR interferometry, phase unwrapping, persistent scatterer interferometry, differential SAR tomography, and data fusion.